Search for Fermiophobic Higgs using the 3γ+X Final State in 1.96-TeV Proton-Antiproton Collisions

Atsunari Hamaguchi

Search for Fermiophobic Higgs using the 3γ+X Final State in 1.96-TeV Proton-Antiproton Collisions

A dissertation submitted
in partial fullfillment of the requirements
for the Degree of Doctor of Philosophy in Science
in the Graduate School of Science of
Osaka City University

by
Atsunari Hamaguchi

January 2012

Abstract

We search for a fermiophobic Higgs boson using 3γ+X events in $p\bar{p}$ collisions at $\sqrt{s}$ = 1.96 TeV. In the Standard Model (SM), the Higgs boson is introduced to explain the electroweak symmetry breaking (EWSB) and the origin of fermion masses. The minimal extension of the SM contains an additional Higgs doublet, the "two Higgs doublet model" (2HDM). In this model a fermiophobic Higgs boson (h_f) which signifies very suppressed or zero coupling to the fermions, may arise in a paticular version of the 2HDM called type I. The data were collected with the CDF-II detector at the Fermilab Tevatron collider and correspond to an integrated luminosity of 6.0 fb^{-1}. We estimate the fake-photon backgrounds and Direct Triphoton Production(DTP) backgrounds. The expected number of signal events is 17.7 for the fermiophobic higgs of the mass 75 GeV/c^2 and $H^{\pm}$ of the mass 120 GeV/c^2. The expected number of backgrounds is 1.9$\pm$0.9, From these results, we obtain the expected limits on $\sigma(p\bar{p} \rightarrow H^{\pm}h_f) \times Br(H^{\pm} \rightarrow W^{*}h_f) \times (Br(h_f \rightarrow \gamma\gamma))^2$ of 8.0 fb for the fermiophobic Higgs of 75 GeV/c^2 and $H^{\pm}$ of the mass 120 GeV/c^2 at the 95% confidence level, while the observed limit is 10 fb.

Acknowledgments

I would like to thank everyone who supported and encouraged me until this thesis is completed for a few years. This thesis could have been not completed without the numerous supports and encouragements.
I would like to thank Prof. Toru Okusawa. He gave me the opportunity to join to the CDF experiment and supported the working during my doctoral program. I am deeply thankful to Prof. Yoshi Seiya. He always elegantly advised me the physical ideas and gave me comments for this analysis. I am specially grateful to Prof. Kazuhiro Yamamoto. He gave me helpful suggestion on matters and supported me technical aspects.
I would like to thank to CDF SUSY group convener, Prof. David Toback. He supported my analysis and empathetically discussed with me to polish the analysis. I am thankful to Prof. Shin-Shan Yu in photon group members who helped me.
CDF consumer group members, Prof. Kaori Maeshima, Dr. Pasha Murat, and other staffs, I was happy and did valuable experience by working with them.
I would like to express thanks to Ms. Carol Picciolo, Ms. Kyoko Kunori, and Ms. Kazuko Kumashiro. They supported me by a lot of their secretary works and I could concentrate on my working by them. I would like to thank the staff members and the students of CDF Japan group, Prof. Kunitaka Kondo, Prof. Shinhong Kim, Prof. Fumihiko Ukegawa, Prof. Kazuhiko Hara, Prof. Yuji Takeuchi, Prof. Makoto Shimojima, Prof. Yukihiro Kato, Prof. Kohei Yorita, Dr. Koji Ebina, Dr. Junji Naganoma, Dr. Kimura Naoki, Dr. Koji Sato, Dr. Tomonobu Tomura, Dr. Hideki Miyake, Dr. Masakazu Kurata, Dr. Koji Nakamura, Dr. Takayuki Wakisaka, Dr. Yoshiaki Nagai, Mr. Yuji Sudo, and Mr. Ken-ichi Takemasa. It was greatest delight and full of happiness for me to get through same times with them.

Contents

1 Introduction

Interactions between fundamental particles are mediated by exchanging particles known as force carriers. Calculations along with theories suggesting how they relate are reasonable agreement with the data. However the Higgs particles which is a key building block in these theories has not been observed yet. The Higgs particle plays a unique role by explaining why the other elementary particles are massive.

1.1 The Standard Model

Standard Model (SM) is one of particle physics theories based on gauge field theory which is invariance under the gauge transformation, and extremely well describes the phenomena and properties of the elementary particles which was tested by various experiments. The SM can form three gauge field theories in the framework, the three gauge field theories are "Quantum Electrodynamics (QED)", "Quantum Chromodynamics (QCD)" and "Weak theory". The QED describes the electromagnetic interaction between charged particles based on $U(1)$ gauge group, the QCD describes the strong interaction between quarks and gluons based on $SU(3)_C$ gauge group, and the Weak theory describes weak interaction where in the nuclei based on $SU(2)$ gauge group. In particular, the QED and the Weak theory are unified in the SM framework as $SU(2)_L \otimes U(1)_Y$ gauge theory. In addition, the "Higgs Mechanism" amazingly plays to give "Mass" to a particle with keeping the gauge invariance in the theory. However, a particle is needed for the mechanism, which is called Higgs boson, the Higgs boson is undiscovered yet experimentally.

1.1.1 Elementary Particles in the Standard Model

In the SM, there are mainly 2 types elementary particles, so-called "Fermion" and "Boson", respectively. The Fermions construct matters in the nniverse, while the Bosons mediate forces between the elementary particles. The visible complex matters in this world are made up of them. This following section describes the elementary particles in some detail.

Fermion

A particle called Fermion obeys the "Pauli Exclusion Principle" ,i.e. it has half-integral spin. In the SM, the Fermions are classified into six leptons and six quarks. The three of the six leptons are charged lepton, which are "electron" , "muon", and "tau", they have different mass, respectively, however its spin, weak isospin, and electric charge are same. The remaining three leptons have no electric charge so-called "neutrino", they have a lepton flavor (lepton number) same as corresponding charged lepton, when electron has +1 electron number, the corrsponding neutrino so-called "electron neutrino" has +1 electron number.
The three of the six quarks have 2/3 electric charge, so-called "up", "charm", and

"top" quark respectively, they are collectively called "up-type quark" while the other three quarks is $-1/3$ electric charge called "down", "strange", and "bottom", collectively "down-type quark". They also have color charge which is source of the strong interaction.
In addition, there are antiparticle for each fermion, which have opposite quantum numbers corresponding to the each fermion. Table 1 shows the list of leptons and the quarks.

Boson

The Bosons play a role in mediating force between the elementary particles corresponding to type of forces. Such bosons are especially called "gauge boson". In the present, it is believed that there are at least 4 kind of force, "Electromagnetic", "Weak", "Strong", and "Gravity", however the Gravity force is excluded in the SM due to normalization problem, and its extremely small affect in the particle world. The electromagnetic forces are propagated via "photon" by feeling electric charge which is gauge boson in the electromagnetic field. The photon has spin 1, and massless means that the force carries to infinity. The weak force interactions are mediated by $W^{\pm}$ and Z^0 bosons have 80 and 91 GeV/c^2 mass, respectively, unlike electromagnetic force, it can effect whithin short range ($\sim 10^{-16}$ cm). The strong force interactions are occurred by exchanging gauge boson so-called "gluon" via color charge, which can propagate within finite range due to "asymptotic freedom". The color charge are conventionally expressed as 3 colors, "red (r)", "blue (b)", and "green (g)", which is introduced by taking Pauli Exclusion Principle in Hadrons (Baryons and Mesons) into account, for example Δ^{++} particle is constructed by 3 up-quarks, it can be expressed as (u_r, u_b, u_g). The force mediating particles, i.e. gauge bosons, are shown in Table 2 [1].

1.1.2 Quantum Electrodynamics: $U(1)$

Quantum Electrodynamics (QED) is relativistic quantum field theory of the classical electromagnetism [2]. QED has the structure of an Abelian gauge theory with a $U(1)$ gauge group. The gauge field, which mediates the interaction between the charged 1/2 spin fields, is electromagnetic field. An electron is described by a complex field and the Lagrangian is written as follows,

$$\mathcal{L} = i\bar{\psi}\gamma_\mu\partial^\mu\psi - m\psi\bar{\psi}. \tag{1}$$

The Lagrangian is invariant under the phase transformation,

$$\psi \to e^{i\alpha}\psi, \tag{2}$$

where α is a real constant. The family of phase transformation $U(\alpha) \equiv e^{i\alpha}$ forms a unitary Abelian group known as the $U(1)$ group. Using Neother's theorem, this invariant implies the existence of a conserved current and charge,

$$\partial_\mu j^\mu = 0, j^\mu = -e\bar{\psi}\gamma^\mu\psi, Q = \int d^3x j^0. \tag{3}$$

In addition, the local gauge transformation is generalized as

$$\psi \to e^{i\alpha(x)}\psi, \tag{4}$$

where $\alpha(x)$ depends on space and time in a completely arbitrary way. Now, the Lagrangian (1) is not invariant under such phase transformation. Using (4),

$$\bar{\psi} \to e^{-i\alpha(x)}\bar{\psi}, \tag{5}$$

the last term of the Lagrangian is invariant, however the term of derivative ψ is not as follows,

$$\partial_\mu\psi \to e^{i\alpha(x)}\partial_\mu\psi + ie^{i\alpha(x)}\psi\partial_\mu\alpha, \tag{6}$$

and the $\partial_\mu\alpha$ term breaks the invariant of the Lagrangian. To impose invariance of the Lagrangian under local gauge transformation, the derivative ∂_μ is modified as D_μ, the treatment covariantly transforms the Lagrangian under the phase transformation,

$$\begin{aligned} D_\mu\psi &\to e^{i\alpha(x)}D_\mu\psi, & (7)\\ D_\mu &\equiv \partial_\mu - ieA_\mu, & (8) \end{aligned}$$

where a vector field A_μ is introduced to cancel the unwanted term in (6), and the vector field transforms as,

$$A_\mu \to A_\mu + \frac{1}{e}\partial_\mu\alpha. \tag{9}$$

Invariance of the Lagrangian (1) under the local gauge transformation (4) is achieved by replacing ∂_μ by D_μ,

$$\begin{aligned} \mathcal{L} &= i\bar{\psi}\gamma_\mu D^\mu\psi - m\psi\bar{\psi}. \\ &= \bar{\psi}(i\gamma^\mu\partial_\mu - m)\psi + e\bar{\psi}\gamma^\mu\psi A_\mu. \end{aligned} \tag{10}$$

By demanding local phase invariance, it forces to introduce a vector field A_μ, i.e. gauge field in QED. If the additional field is regarded as the physical photon field, the Lagrangian is added a term corresponding to its kinetic energy. Since the kinetic term must be invariant under (9), it can only involve the gauge invariant field strength tensor

$$F_{\mu\nu} = \partial_\mu A_\nu - \partial_\nu A_\mu. \tag{11}$$

Finally, the Lagrangian of QED is expressed as follows,

$$\mathcal{L} = \bar{\psi}(i\gamma^\mu\partial_\mu - m)\psi + e\bar{\psi}\gamma^\mu\psi A_\mu - \frac{1}{4}F_{\mu\nu}F^{\mu\nu}. \tag{12}$$

The addition of a mass term $(1/2)m^2A_\mu A^\mu$ is prohibited by gauge invariance. The gauge particle must be massless and the gauge field can propagate to an infinite range.

1.1.3 Quantum Chromodynamics: $SU(3)_C$

Quantum Chromodynamics (QCD) is the gauge theory for strong interactions [2]. QCD is based on the extension of the QED idea, however it has a gauge transformation invariant nunder $SU(3)$ group on quark color fields. The Lagrangian is written in the following,

$$\mathcal{L} = \bar{q_j}(i\gamma^\mu \partial_\mu - m)q_j, . \tag{13}$$

where $q_j (j = 1, 2, 3)$ denotes the three color fields. The Lagrangian (13) is to be invariant under local phase transformations as follows,

$$q(x) \rightarrow Uq(x) \equiv e^{i\alpha_a(x)T_a} q(x), \tag{14}$$

where U is an arbitrary 3×3 unitary matrix, it has the summation over the repeated suffix a. $T_a (a = 1, \ldots, 8)$ is a set of linearly independent traceless 3×3 matrices, and α_a are the group parameters. The group is non-Abelian since the generators T_a do not commute with each other,

$$[T_a, T_b] = if_{abc}T_c, \tag{15}$$

where f_{abc} are real constants called the structure constants of the group. To impose $SU(3)$ local gauge invariance on the Lagrangian (13), the infinitesimal phase transformation is introduced,

$$\begin{aligned} q(x) &\rightarrow [1 + i\alpha_a(x)T_a]q(x), & (16)\\ \partial_\mu q &\rightarrow (1 + i\alpha_a T_a)\partial_\mu q + iT_a q \partial_\mu \alpha_a. & (17) \end{aligned}$$

The last term spoils the invariance of Lagrangian. The 8 gauge fields G^a_μ are constructed by reequiring the invariant of the Lagrangian under the local gauge transformation,

$$G^a_\mu \rightarrow G^a_\mu - \frac{1}{g}\partial_\mu \alpha_a - f_{abc}\alpha_b G^c_\mu, \tag{18}$$

and form a covariant derivative,

$$D_\mu = \partial_\mu + igT_a G^a_\mu. \tag{19}$$

The gauge invariant QCD Lagrangian is formed by the replacement $\partial_\mu \rightarrow D_\mu$ in the Lagrangian (13), and adding a gauge invariant kinetic energy term for each of the G^a_μ fields,

$$\begin{aligned} \mathcal{L} &= \bar{q}(i\gamma^\mu \partial_\mu - m)q - g(\bar{q}\gamma^\mu T_a q)G^a_\mu - \frac{1}{4}G^a_{\mu\nu}G^{\mu\nu}_a, & (20)\\ G^a_{\mu\nu} &= \partial_\mu G^a_\nu - \partial_\nu G^a_\mu - g f_{abc} G^b_\mu G^c_\nu, & (21) \end{aligned}$$

(20) is the Lagrangian for interacting colored quarks q and vector gluons G_μ, with coupling specified by g. The local gauge invariance requires the gluons to be massless. The field strength $G^a_{\mu\nu}$ has a remarkable new property as shown in the last term in (21). Imposing the gauge symmetry has required that the kinetic energy term in Lagrangian is not purely kinetic but includes an induced self-interaction between the gauge bosons and reflects the fact that gluons themselves carry color charge.

1.1.4 Electroweak Theory: $SU(2)_L \otimes U(1)_Y$

The electroweak theory is a gauge theory unified the electromagnetic $U(1)$ and weak interactions $SU(2)$. The weak interaction typically occurs in β decay in nuclei ($n \rightarrow p + l + \nu_l$) via W boson which is weak gauge boson. The weak interaction acts only left-handed fermions, so-called $V - A$ structure, and based on $SU(2)$ isospin group with three vector bosons.
By demanding weak interaction, the quark field are expressed as follows,

$$\psi_L = \begin{pmatrix} q_u \\ q_d \end{pmatrix}_L, \psi_R = q_R. \tag{22}$$

The left-handed quark fields can be expressed in doublets, while the right-handed quark fields in singlets, where q_u is up-type quarks (u,c,t), q_d is down-type quarks (d,s,b), and q_R is six quark flavours (u,d,c,s,t,b). The lepton fields are also expressed by,

$$\psi_L = \begin{pmatrix} \nu_l \\ l^- \end{pmatrix}_L, \psi_R = l_R. \tag{23}$$

where l means three lepton flavours i.e. e, μ, and τ. Note that there are no right-handed neutrino fields due to satisfying $V - A$ structure in the weak interaction. Here, the free Lagrangian for the lepton and the quark fields is written in,

$$\mathcal{L} = \sum_{j=L,R} i\bar{\psi}_j \gamma^\mu \partial_\mu \psi_j. \tag{24}$$

The Lagrangian (24) is invariant under global transformation,

$$\psi_L \rightarrow e^{i\alpha_a T^a + i\beta Y} \psi_L, \tag{25}$$
$$\psi_R \rightarrow e^{i\beta Y} \psi_R, \tag{26}$$

where the parameter Y is hypercharge for $U(1)_Y$ phase transformation, the T^a is defined by using Pauli matrices as follows,

$$T^a = \frac{\tau^a}{2}, \tau^1 = \begin{pmatrix} 0 & 1 \\ 1 & 0 \end{pmatrix}, \tau^2 = \begin{pmatrix} 0 & -i \\ i & 0 \end{pmatrix}, \tau^3 = \begin{pmatrix} 1 & 0 \\ 0 & -1 \end{pmatrix}, \tag{27}$$

and it is under $SU(2)_L$ transformation. The Lagrangian should be invariant under local $SU(2)_L \otimes U(1)_Y$ gauge transformation,

$$\psi_L \rightarrow e^{i\alpha_a(x) T^a + i\beta(x) Y} \psi_L, \tag{28}$$
$$\psi_R \rightarrow e^{i\beta(x) Y} \psi_R, \tag{29}$$

To achieve the local gauge invariance in the Lagrangian, the derivative is raplaced by covariant derivatives,

$$D_{\mu L} \equiv \partial_\mu + igT_a W_\mu^a + i\frac{g'}{2} B_\mu Y \tag{30}$$

$$D_{\mu R} \equiv \partial_\mu + i\frac{g'}{2} B_\mu Y \tag{31}$$

$D_{\mu L}(D_{\mu R}$ is for the left (right)-handed fermion field, g is the coupling constant of $SU(2)_L$ and g' is of $U(1)_Y$. The covariant derivatives have gauge fields, $W^a_\mu(a = 1, 2, 3)$ for $SU(2)_L$, and B_μ for $U(1)_Y$. The gauge field also transform as,

$$B_\mu \rightarrow B_\mu - \frac{1}{g'}\partial_\mu \beta, \tag{32}$$

$$\boldsymbol{W} \rightarrow \boldsymbol{W}_\mu - \frac{1}{g'}\partial_\mu \boldsymbol{\alpha} - \boldsymbol{\alpha} \times \boldsymbol{W}_\mu \tag{33}$$

In addition, the gauge field strength tensors are introduced by requiring the local gauge invariant,

$$B_{\mu\nu} \equiv \partial_\mu B_\nu - \partial_\nu B_\mu, \tag{34}$$

$$W^a_{\mu\nu} \equiv \partial_\mu W^a_\nu - \partial_\nu W^a_\mu - g\epsilon_{abc} W^b_\mu W^c_\nu. \tag{35}$$

Finally , the Lagrangian under local gauge invariant in electroweak interaction can be written as,

$$\mathcal{L} = \sum_{j=L,R} i\bar{\psi}_j \gamma^\mu D_{\mu,j}\psi_j - \frac{1}{4}W^a_{\mu\nu}W^{\mu\nu}_a - \frac{1}{4}B_{\mu\nu}B^{\mu\nu}, \tag{36}$$

Although the weak and electromagnetic interactions coexist in the $SU(2)_L \otimes U(1)_Y$ gauge symmetry, it describes no realistic world, because there are no mass terms for fermions and weak gauge bosons which are know that they are massive, and weak interaction only affects in short range. However introducing the mass terms such also break due to different transformation between the left-handed and right-handed fermion fields,

$$m_f \bar{f} f = m_f(\bar{f}_R f_L + \bar{f}_L f_R), \tag{37}$$

using the left-handed and right handed relation equations,

$$f_L = \frac{1}{2}(1 - \gamma^5)f, f_R = \frac{1}{2}(1 + \gamma^5)f. \tag{38}$$

Fortunately, the nature have a solution (mechanism) to be invariant under gauge transformation when the Lagrangian has a mass terms for fermion and weak gauge boson, so-called "Spontaneous symmetry breaking".

1.1.5 Spontaneous Symmetry Breaking

To give mass to the gauge bosons and fermions, the electroweak gauge symmetry are hidden. Here let us start by introducing the scalar real field ϕ as simple example, and its Lagrangian is written by,

$$\mathcal{L} = \frac{1}{2}\partial_\mu \phi \partial^\mu \phi - V(\phi), \tag{39}$$

$$V(\phi) = \frac{1}{2}\mu^2\phi^2 + \frac{1}{4}\lambda\phi^4, \tag{40}$$

where $\lambda > 0$, the Lagrangian is invariant under the symmetry operation:$\phi \rightarrow -\phi$.
If $\mu^2 > 0$, it can be regarded that the Lagrangian describes a scalar fields with mass μ, the ϕ^4 terms mean self-interaction with coupling λ, and the minimum of the potential $V(\phi)$ is,

$$\langle 0|\phi|0\rangle \equiv \phi^0 = 0. \tag{41}$$

On the other hand, if $\mu^2 < 0$, the potential $V(\phi)$ has a minimum when,

$$\frac{\partial V}{\partial \phi} = \mu^2\phi + \lambda\phi^3 = 0, \tag{42}$$

$$\langle 0|\phi|0\rangle \equiv \phi_0^2 = -\frac{\mu^2}{\lambda} \equiv v^2. \tag{43}$$

The value $v = \sqrt{\mu^2/\lambda}$ is called "vacuum expectation value" of the scalar field ϕ. Here the field ϕ is expanded around the minimum value v with the quantum fluctuation η,

$$\phi = v + \eta. \tag{44}$$

From this, the Lagrangian (40) becomes

$$\mathcal{L} = \frac{1}{2}\partial_\mu\eta\partial^\mu\eta - \lambda v\eta^3 - \frac{1}{4}\eta^4 + const, \tag{45}$$

where a scalar field η with mass $m_\eta = \sqrt{-2\mu^2}$ appears in the Lagrangian (45), and there are self-interaction terms η^3 and η^4, in particular, the cubic term breaks the symmetry in the Lagrangian without external operation, it is called "Spontaneous Symmetry Breaking (SSB)". Next step, let us introduce the SSB to electroweak symmetry to get the true world picture, that is, the weak bosons and fermions are massive.

1.1.6 Higgs Mechanism

As described in 1.1.4, however the Lagrangian (36) is invariant local gauge invariant, the Lagrangian describes the no real world picture because the weak gauge bosons and fermions have no mass in the Lagrangian. But the Lagrangian is broken by including the mass terms. Now, let us show that the Lagrangian becomes the real world Lagrangian by using the symmetry breaking [6, 7, 8]. By introducing complex scalar doublet,

$$\phi = \begin{pmatrix} \phi^+ \\ \phi^0 \end{pmatrix} = \frac{1}{\sqrt{2}}\begin{pmatrix} \phi_1 + i\phi_2 \\ \phi_3 + i\phi_4 \end{pmatrix}, Y_\phi = +1, \tag{46}$$

where the hypercharge is 1 for the scalar field, the Lagrangian can be written by

$$\mathcal{L} = (\partial_\mu\phi)^\dagger(\partial^\mu\phi) - \mu^2\phi^\dagger\phi - \lambda(\phi^\dagger\phi)^2. \tag{47}$$

In this case, If $\mu^2 < 0$, the vacuum expectation value and the scalar field after the symmetry breaking with the real scalar field h become as follow,

$$\begin{aligned} \phi^\dagger\phi &= \frac{\phi_1^2+\phi_2^2+\phi_3^2+\phi_4^2}{2} = \frac{-\mu^2}{2\lambda} \equiv \frac{v^2}{2}, && (48)\\ \phi &= \frac{1}{\sqrt{2}}\begin{pmatrix} 0 \\ v+h \end{pmatrix}, && (49) \end{aligned}$$

where the scalar fields are chosen as $\phi^1 = \phi^2 = \phi^4 = 0$, and $\phi^3 = v$. Let us expand the first term of the Lagrangian (47), i.e. the kinematical terms,

$$\begin{aligned} |D_\mu\phi|^2 &= |(\partial_\mu - igT^aW_\mu^a + i\frac{g'}{2}B_\mu)\phi|^2 \\ &= \frac{1}{2}(\partial_\mu h)^2 + \frac{g^2v^2}{4}\left|\frac{W_\mu^1+iW_\mu^2}{2}\right|^2 + \frac{v^2}{8}|gW_\mu^3 - g'B_\mu|^2 \\ &+ \text{interaction terms} \end{aligned} \quad (50)$$

where the derivative is replaced to covariant derivative (31), and define the field $W_\mu^\pm$, Z_μ, and A_μ written as follows,

$$\begin{aligned} W_\mu^\pm &= \frac{1}{\sqrt{2}}(W_\mu^1 \pm iW_\mu^2), && (51)\\ Z_\mu &= W_\mu^3\cos\theta_W - B_\mu\sin\theta_W, && (52)\\ A_\mu &= W_\mu^3\sin\theta_W + B_\mu\cos\theta_W, && (53)\\ & && (54) \end{aligned}$$

where weak mixing angle θ_W is defined as $g' = g\tan\theta_W$, the A_μ field is the orthogonal field to the Z_μ field, and the masses of fields can be expressed as respectively,

$$M_W = \frac{1}{2}vg, M_Z = \frac{1}{2}\sqrt{g^2+g'^2}, M_A = 0. \quad (55)$$

Note that the W_μ and the Z_μ fields become massive, while the A_μ field is still massless, that is, the weak gauge bosons can have desirable mass by introducing the SSB, in particular, it is called "Higgs Mechanism". By using the weak mixing angle θ_W, the W_μ field is related to $Z\mu$ field as follows,

$$M_W = M_Z\cos\theta_W. \quad (56)$$

The fermion fields should be massive to achieve the true world in the electroweak Lagrangian. The Higgs mechanism also gives a mass to the fermions under the local gauge invariant. The Lagrangian with fermion fields is written by,

$$\mathcal{L}_{Yukawa} = -G_f\bar{\psi}_L\phi\psi_R - G_f\bar{\psi}_R\phi^\dagger\psi_L, \quad (57)$$

where G_f is arbitrary constant for each fermion. First, the lepton sector Lagrangian becomes,

$$\begin{aligned}\mathcal{L}_{lepton} &= -G_l\left[(\bar{\nu},\bar{l})_L\begin{pmatrix}\phi^+\\ \phi^0\end{pmatrix}l_R+\bar{l}_R(\psi^-,\bar{\psi^0}\begin{pmatrix}\nu_l\\ l\end{pmatrix}_L\right]\\ &= -\frac{G_l}{\sqrt{2}}v(\bar{l}_Ll_R+\bar{l}_Rl_L)-\frac{G_l}{\sqrt{2}}(\bar{l}_Ll_R+\bar{l}_Rl_L)h\\ &= -m_l\bar{l}l-\frac{m_l}{v}\bar{l}lh, \end{aligned} \tag{58}$$

using (38) and $m_l = G_l v/sqrt2$ is defined as the lepton mass. The lepton sector Lagrangian (58) then keeps the gauge symmetry under the local transformation. Let us show that the quark sector Lagrangian also become the invariant. In the quark sector, the new higgs doublet must be introduced by using ϕ to give the up-type quark mass,

$$\phi_c = i\tau_2\phi = \begin{pmatrix}-\bar{\phi^0}\\ \phi^-\end{pmatrix}, \tag{59}$$

the higgs doublet is chosen the following after the symmetry breaking,

$$\phi_c = \frac{1}{\sqrt{2}}\begin{pmatrix}v+h\\ 0\end{pmatrix}. \tag{60}$$

The quark sector Lagrangian is formed by

$$\begin{aligned}\mathcal{L}_{quark} &= -G_d(\bar{u},\bar{d})_L\begin{pmatrix}\psi^+\\ \psi^0\end{pmatrix}d_R-G_u(\bar{u},\bar{d})_L\begin{pmatrix}-\bar{\psi^0}\\ \psi^-\end{pmatrix}u_R+h.c.\\ &= -m_d\bar{d}d-m_u\bar{u}u-\frac{m_d}{v}\bar{d}dh-\frac{m_u}{v}\bar{u}uh. \end{aligned} \tag{61}$$

where the down-type and the up-type quark masses are defined as $m_d = G_d v/\sqrt{2}$ and $m_u = G_u v/\sqrt{2}$ respectively. The quark sector Lagrangian alse preserves the gauge invariant after the symmetry breaking.
The Higgs Mechanism gives us the electroweak Lagrangian with relevant field mass terms under the gauge symmetry. However the fermions masses are not predicted in the Higgs mass and its potential structrue are alse unknown. They need to be revealed by an experiment.

1.1.7 Two Higgs Doublet Model

In the previous section, the minimal SM higgs is considered, however the scalar field doublet can be introduced as two, and more doublets to break the electroweak symmetry. Then, Let us introduce the two complex doublet scalar fields ϕ_1 and ϕ_2 so-called "Two Higgs Doublet Model (2HDM)",

$$\phi_1 = \begin{pmatrix}\phi_1^+\\ \phi_1^0\end{pmatrix},\ \phi_2 = \begin{pmatrix}\phi_2^+\\ \phi_2^0\end{pmatrix}, \tag{62}$$

The 2HDM have mainly two scenarios, named "Type-I" and "Type-II", respectively. In the "Type-I", the scalar fields ϕ_1 do not couple to any quarks and leptons, while the other scalar fields ϕ_2 couple to them. In the "Type-II", the first scalar fields ϕ_1 couple only to down-type quarks and leptons, while the second scalar fields ϕ_2 couple only to up-type quarks. In this thesis, the Type-I scenario is noticed [9, 10].

First, let us start to introduce the most general potential written as,

$$\begin{aligned} V(\phi_1,\phi_2) &= \lambda_1(\phi_1^\dagger\phi_1 - v_1^2)^2 + \lambda_2(\phi_2^\dagger\phi_2 - v_2^2)^2 \\ &+ \lambda_3\left[(\phi_1^\dagger\phi_1 - v_1^2) + (\phi_2^\dagger\phi_2 - v_2^2)\right]^2 \\ &+ \lambda_4\left[(\phi_1^\dagger\phi_1)(\phi_2^\dagger\phi_2) - (\phi_1^\dagger\phi_2)(\phi_2^\dagger\phi_1)\right] \\ &+ \lambda_5\left[\mathrm{Re}(\phi_1^\dagger\phi_2) - v_1v_2\cos\xi\right]^2 + \lambda_6\left[\mathrm{Im}(\phi_1^\dagger\phi_2) - v_1v_2\sin\xi\right]^2 \\ &+ \lambda_7\left[\mathrm{Re}(\phi_1^\dagger\phi_2) - v_1v_2\cos\xi\right]\left[\mathrm{Im}(\phi_1^\dagger\phi_2) - v_1v_2\sin\xi\right] \end{aligned} \tag{63}$$

where λ_i are real parameters, and the potential has a discrete symmetry, $\phi_1 \to -\phi_1$, only broken softly. The last term with λ_7 can be eliminated by defining the phases of the scalar fields or demanding the CP-conservation which is assumed in this section.

The vacuum expectation values for the two scalar fields after symmetry breaking are formed as follows,

$$\langle\phi_1\rangle = \begin{pmatrix} 0 \\ v_1 \end{pmatrix},\ \langle\phi_2\rangle = \begin{pmatrix} 0 \\ v_2 \end{pmatrix}, \tag{64}$$

where $v_{1,2}$ are real, in addition, the vacuum expectation values are defined by,

$$\tan\beta \equiv \frac{v_2}{v_1},\ v^2 \equiv v_1^2 + v_2^2 = \frac{2m_W^2}{g^2} = (173\ \mathrm{GeV})^2, \tag{65}$$

as discussed below, the parameter β serves as key role in the model. In this model, there are five Higgs boson (h^0, H^0, A^0, and $H^\pm$) and three Goldstone bosons (G^0 and $G^\pm$) which give a mass to weak bosons. The charged Goldstone boson $G^\pm$ is orthogonal to the charged Higgs boson $H^\pm$, and the charged sector are expressed by,

$$G^\pm = \phi_1^\pm\cos\beta + \phi_2^\pm\sin\beta, \tag{66}$$

$$H^\pm = -\phi_1^\pm\sin\beta + \phi_2^\pm\cos\beta. \tag{67}$$

By demanding the CP-conservation, the imaginary parts and the real parts of the neutral scalar fields decouple. The neutral Goldstone boson is orthogonal to the one of the neutral higgs bosons, the imaginary sector (CP-odd) are obtained as,

$$G^0 = \sqrt{2}\left[\mathrm{Im}(\phi_1^0)\cos\beta + \mathrm{Im}(\phi_2^0)\sin\beta\right], \tag{68}$$

$$A^0 = \sqrt{2}\left[-\mathrm{Im}(\phi_1^0)\sin\beta + \mathrm{Im}(\phi_2^0)\cos\beta\right], \tag{69}$$

while the real sector (CP-even) are expressed by as follows,

$$H^0 = \sqrt{2}\left[(\mathrm{Re}(\phi_1^0)-v_1)\cos\alpha+(\mathrm{Re}(\phi_2^0)-v_2)\sin\alpha\right], \quad (70)$$

$$h^0 = \sqrt{2}\left[-(\mathrm{Re}(\phi_1^0)-v_1)\sin\alpha+(\mathrm{Re}(\phi_2^0)-v_2)\cos\alpha\right], \quad (71)$$

where the neutral higgs scalars are related with the mixing angle α which is defined as,

$$\sin 2\alpha = \frac{2\mathcal{M}_{12}}{\sqrt{(\mathcal{M}_{11}-\mathcal{M}_{22})^2+4\mathcal{M}_{12}^2}}, \quad (72)$$

$$\cos 2\alpha = \frac{\mathcal{M}_{11}-\mathcal{M}_{22}}{\sqrt{(\mathcal{M}_{11}-\mathcal{M}_{22})^2+4\mathcal{M}_{12}^2}}, \quad (73)$$

then, the scalar masses can be obtained by diagonalizing the Higgs boson matrix, $M_{ij}^2=\frac{\partial^2 V}{\partial\phi_i\partial\phi_j}$, the Higgs masses are respectively written as,

$$M_{H^0,h^0}^2 = \frac{1}{2}\left[\mathcal{M}_{11}+\mathcal{M}_{22}\pm\sqrt{(\mathcal{M}_{11}-\mathcal{M}_{22})^2+4\mathcal{M}_{12}^2}\right], \quad (74)$$

$$M_{H^\pm}^2 = \lambda_4(v_1^2+v_2^2),\ M_{A^0}^2=\lambda_6(v_1^2+v_2^2), \quad (75)$$

where using the mass matrices defined as follows,

$$\mathcal{M}=\begin{pmatrix}\mathcal{M}_{11} & \mathcal{M}_{12}\\ \mathcal{M}_{12} & \mathcal{M}_{22}\end{pmatrix}=\begin{pmatrix}4v_1^2(\lambda_1+\lambda_3)+v_2^2\lambda_5 & (4\lambda_3+\lambda_5)v_1v_2\\ (4\lambda_3+\lambda_5)v_1v_2 & 4v_2^2(\lambda_2+\lambda_3)+v_1^2\lambda_5\end{pmatrix}. \quad (76)$$

The neutral Higgs boson couplings relate to the vacuum expectation value ratio β and the mixing angle α, the coupling can be repressed by,

$$\frac{g_{h^0VV}}{g_{\phi^0VV}}=\sin(\beta-\alpha),\ \frac{g_{H^0VV}}{g_{\phi^0VV}}=\cos(\beta-\alpha), \quad (77)$$

where ϕ^0 is minimal SM Higgs boson, and $V=W^\pm,Z$. Note that the remaining neutral Higgs boson A^0 couples to no gauge boson.

Next, let us show the Higgs-fermion interaction in the Type-I. The interaction is formed as,

$$\begin{aligned}\mathcal{L}_{\mathrm{fermion}} = &-\frac{g}{2M_W\sin\beta}\bar{D}M_DD(H^0\sin\alpha+h^0\cos\alpha)-\frac{ig\cot\beta}{2M_W}\bar{D}M_D\gamma^5DA^0\\ &-\frac{g}{2M_W\sin\beta}\bar{U}M_UU(H^0\sin\alpha+h^0\cos\alpha)+\frac{ig\cot\beta}{2M_W}\bar{U}M_U\gamma^5UA^0\\ &+\frac{g\cot\beta}{2\sqrt{2}M_W}(\bar{U}[M_UK(1-\gamma^5)-KM_D(1+\gamma^5)]DH^++h.c.)\\ &+\text{leptonic sector.}\end{aligned} \quad (78)$$

where M_U and M_D are diagonal quark matrices, K is Kobayashi-Maskawa mixing matrix. The Higgs-lepton couplings can be expressed by replacing U, D and the quark

mass matrices with the corresponding lepton fields and lepton matrices and setting $K = 1$. The neutral Higgs boson couplings to gauge bosons and fermions are shown in Table 3. In particular, the "fermiophobic Higgs (h_F)" appears in the 2HDM Type-I by setting the mixing angle,

$$\alpha = \frac{\pi}{2}, \tag{79}$$

as seen in (78), so-called "fermiophobia". The "fermiophobic Higgs" becomes only coupling to the bosons.

2 Experimental Apparatus

This analysis was performed using the Collider Detector at Fermilab (CDF), a general purpose experiment designed to study proton-antiproton collisions at $sqrt(s) = 1.96$ TeV. In this section, the Tevatron accelerator (proton-antiproton collider) and the CDF detector are described.

2.1 Tevatron Accelerator

The Tevatron is the proton antiproton accelerator at Fermi National Accelerator Laboratory. Its schematic layout is shown in Figure 1. Proton and antiprotons collide at a center-of-mass energy of $\sqrt{s} = 1.96$ TeV.

2.1.1 Preacc

The Pre-accelerator (Preacc) is the Cockcroft-Walton style electrostatic Pre-accelerator. It converts hydrogen gas to ionized hydrogen gas and accelerates to an energy to 750 keV.
Gaseous hydrogen is extracted from a small tank and injected into the ion source, out of which emerges H^- ions. These ions are extracted from the source at 18 keV and transferred to a Cockcroft-Walton electrostatic pre-accelerator (Preacc), which accelerates H^- to 750 keV. The acceleration process can be thought of roughly in the following terms: the dome containing H^- ions is held at an electric potential of 750 keV; a column to achieve the final energy of 750 keV. According to nominal specifications, the source-accelerator system gives rise to pulses of H^- of current of 50 mA and pulse length of 30 seconds.

2.1.2 Linac

The Linear Accelerator (Linac) is the next level of acceleration and consists of a series of drift tubes. It takes 750 keV hydrogen ions to 400 MeV. The Linac consists of two main sections, the low energy drift tube Linac and the high-energy side coupled cavity Linac. The drift tube Linac makes up the first five radio-frequency (RF) stations. A

large power amplifier tube posers each drift tube. These tubes amplify the 201 MHz RF signal used to drive the low energy cavities and accelerate H^- to 116 MeV. The last nine cavities are Klystron amplifiers operating at 805 MHz. The Linac can accelerate beam once every 66 milliseconds (a 15 Hz repetition rate).

2.1.3 Booster

The Booster consists of a series of magnets around 75 meters in radius with 18 RF cavities interspersed. The Booster is made up of 96 combined function magnets in a series of 24 repeating periods. Their magnetic field varies from about 740 gauss at injection to 7,000 gauss at extraction. The Booster tunnel is a concrete tunnel 8 feet high and 10 feet wide, covered by 15 feet of earth shielding. It strips off electrons from 400 MeV hydrogen ion and makes proton accelerate to 8 GeV. The ionized hydrogen beam passes through a carbon foil which removes the electrons leaving bare protons.

2.1.4 Main Injector

The Main Injector is a circular synchrotorn. It can accelerates 8 GeV proton to 120 GeV or 150 GeV. The Main Injector has 18 accelerating cavities. As well as accepting protons from the Booster, the Main Injector can accept antiprotons from the Antiproton Source. The Main Injector can accelerate beam as fast as every 2.2 seconds.

2.1.5 $\bar{p}$ Production

The 120 GeV beam extracted from the Main Injector strikes a nickel target. Out of the spray of random secondary particles, 8 GeV antiprotons are taken.
The largest bottleneck in a proton-antiproton collider is the time required to accumulate the required number of antiprotons. The process is inherently ineffcient. Typically for every 10^5 protons striking a target, only one or two antiprotons are captured and stored. The antiproton source is comprised of a target station, two rings called the Debuncher and Accumulator. The incident beam is focused to a small spot size using a series of quadrupole magnets. The beam strikes the nickel production target. The resulting cone of secondary particles is focused and rendered parallel by means of a Lithium lens known as the "Collection Lens". A pulsed dipole magnet bends all negatively-charged particles of approzimately 8 GeV kinetic energy into the line to the Debuncher while most of the other particles are absorbed within a beam dump. The survived particles are injected into the Debuncher where the momentum spread of the 8 GeV beam of secondaries is redued. Just before the next pulse arrives from the target, the antiprotons are extracted from the Debuncher and injected into the Accumulator. The purpose of the Accumulator is to accumulate antiprotons. This is accomplished by momentum stacking auccessive pulses of antiprotons from the Debuncher ever several hours or days. Both RF and cooling systems are used in the momentum stacking process. The RF decelerates the recently injected pulses of antiprotons from the injection energy.

Cooling systems keep the antiprotons at teh desired momentum and minimize the transverse beam size.

2.1.6 Tevatron

The Tevatron is a circular synchrotron with a circumference of approximately 4 miles. It accelerates protons or antiproton from 150 GeV to 980 GeV. It receive 36 proton and 36 antiproton bunches with a minimum spacing of 392 ns. The protons and antiprotons share the same ring and move in the opposite directions.

2.2 CDF Detector

The data used in this analysis was collected with the Collider Detector at Fermilab (CDF) [11]. The CDF detector is a complex device that consists of many subdetectors as shown in Figure 2 and Figure 3. It is cylindrically symmetric around the beam axis and forward-backward symmetric about the interaction region. It is a general purpose solenoidal detector which combines precision charged particle tacking with fast projective calorimetry and fine grained muon detection. Tracking systems are contained in a superconduction solenoid, 1.5 m in radius and 4.8 m in length, which generates a 1.4 T magnetic field parallel to the beam axis. Calorimetry and muon systems are all located outside the solenoid. We use a coordinate system where the polar angle θ is mesured from the proton direction, the azimuthal angle ϕ is mesured from the horizontal plane going toward the outside of the Tevatron, and the pseudo-rapidity is defined as $\eta = -\ln(\tan(\theta/2))$.

2.2.1 Tracking System

Silicon Detectors

The silicon detector system provides high precision tracking of charged particles near the interaction point. The silicon tracking system consists of three subdetectors, Layer00 (L00), the Silicon Vertex Detector (SVX II) and the Intermediate Silicon Layers detector (ISL). Figure 4 illustrates the silicon detector geometry in the plane transverse to the beam axis.

L00 is placed in the innermost part at a radius of 1.35 cm [12, 13]. It consists of single-sided micro-strip silicon detectors. The position resolution is 21 μm for low p_T (2-3 GeV/c) track and 11 μm for high p_T track.

SVX II is placed outside of L00 [14]. The radial coverage is from 2.4 cm to 10.7 cm and the total length is 96 cm. It consists of three barrels. Each barrel has five layers of double-sided silicon micro-strip detector. Rapidity coverage is $|\eta| < 2.0$. The resolution is 12 μm.

ISL is located between SVX II and COT [15]. It consists of the central detector at radius of 23 cm, and the two forward detectors at radius from 20 cm and 29 cm. The impact parameter resolution is 40 μm using both SVX and ISL. The collision location in z-axis (Z_0) resolution is 70 μm using both SVX and ISL.

Central Outer Tracker (COT)

Outside of the silicon detector, the Central Outer Tracker (COT) covers the region $|\eta| < 1$ with a radial range from 40 cm to 137 cm [16]. It is the drift chamber filled with a gas mixture of Argon 50%, Ethane 35%, and CF_4 15%. Figure 5 illustrates the COT detector geometry. COT has 96 layers grouped into eight super-layers. Each super layer consists of 12 sense wires and 13 potential wires. Four stereo super-layers and four axial super-layers are placed with crossing angle $\pm 2°$. Hit position resolution is about 140 micro-meters. The momentum resolution is $\sigma_{p_T}/p_T^2 = 0.015(\mathrm{GeV}/c)^{-1}$ in high p_T region.

2.2.2 Calorimeters

Calorimeters are used to measure the energy of both charged and neutral particles. The CDF calorimeter consists of two sections: a central barrel calorimeter ($|\eta| < 1.1$) and the forward end-plug calorimeter ($1.1 < |\eta| < 3.6$).

Central Electromagnetic Calorimeter (CEM)

The Central Electromagnetic Calorimeter is a lead-scintillator sampling calorimeter system with projective tower geometry shown in Figure 6. Each tower covers 15° in ϕ. It covers $|\eta| < 1.1$ [17]. The energy resolution σ_E/E is $13.5\%/\sqrt{(E(GeV))}$.

Central Shower Max Detector (CES)

Proportional chambers (CES) are embedded in the electromagnetic section of the central electromagnetic calorimeter at a depth of 6 radiation length (X_0), corresponding to the region of maximum shower intensity for electrons and photons. The position resolution is 0.2 cm at 50 GeV. High-precision position measurements at shower maximum provide track linking ability and transverse shower profiles to improve particle identification. It consists of 48 modules in total, one for each CEM wedge. Each module contains 32 wires parallel to the beam axis and split in the middle for a total of 64 wire readout channels per module, and 128 strips in the direction orthogonal to the wires. Each wedge view is shown Figure 6.

Central Preradiator Detector

CPR helps discrimination between electromagnetic and hadronic showers. It uses a proportional chambers to sample the early development of the shower to measure conversions in the coil, helping to distinguish prompt photons and electrons from photons

originating from π^0 decay and electrons from conversions. A prompt photon has a 60% probability of converting while the conversion probability of at least one photon from $\pi^0 \to \gamma\gamma$ is about 80%.

Central Hadron Calorimeter (CHA)

The Central Hadron Calorimeter is a steel-scintillator sampling calorimeter system [18]. It measures the energy of hadronic showers in the central region. The energy resolution σ_E/E is $50\%/\sqrt{(E(GeV))}$. It is located in the central detector outside of CEM, and covers the pseudo-rapidity range of $|\eta| < 0.9$, 32 layers deep. It consists of 384 towers in total, organized into 24 wedges in ϕ and 8 tower groups in η on each side. Each tower is read out by two PMTs.

Plug Electromagnetic Calorimeter (PEM)

Figure 7 shows the cross section of plug calorimeter system [19]. The Plug Electromagnetic Calorimeter is a lead-scintillator sampling system. It covers $1.1 < |\eta| < 3.6$. A total thickness is about 21 X_0 (radiation length). The energy resolution is $14.4\%/\sqrt{(E(GeV))}$ with a 0.7% constant term.

Plug Shower Max Detector (PES)

The Plug Shower Max Detector is located at the depth of the electromagnetic shower maximum (approximately 6 X_0) and is made of the two layers of 5 mm scintillator strips, with one layer having a 45° crossing angle relative to the other. The two layers are called U and V.

Plug Hadron Calorimeter (PHA)

The Plug Hadron Calorimeter is a steel-scintillator sampling system. The energy resolution is $80\%/\sqrt{(E(GeV))}$.

2.2.3 Muon Chambers

Muon detector coverage is shown in Figure 8. The muon systems consist of four separated subsystems: the central muon chambers (CMU), the central muon upgrade (CMP), the central muon extension (CMX), the barrel muon detector (BMU). The central muon systemis capable of detecting muons with transverse momentum $p_T > 1.4$ GeV/c, through their interaction with the gas and subsequent drift on the produced electrons toward the anode wires.

Central Muon Detector (CMU)

Outside of Central Hadron Calorimeter, the Central Muon Detector (CMU) is located. It covers $|\eta| < 0.7$ at a radial distance of 3470 mm. The muon chamber operate with

argon 50% and ethane 50% gas. A stainless steel 50 μm sense wire is located at the center of cell. Figure 9 illustrates the layout of the central muon chamber. A single hit TDC is used for measurements in the drift time. An rms resolution of 250 μm in the drift direction and an rms resolution of 1.2 mm along the sense wire are attainable.

Central Muon Upgrade Detector (CMP)

The Central Muon Upgrade Detector (CMP) is located behind an additional 60 cm of steel. It covers $|\eta| < 0.6$. It provides confirmation for CMU tracks but with reducedd non-muon (hadronic) background. It consists of 4 layers of single-wire drift cells.

Central Muon Extension Detector (CMX)

The Central Muon Extension (CMX) is located at each end of the central detector. It covers $0.6 < |\eta| < 1.0$.

2.2.4 Luminosity Monitor (CLC)

The Luminosity Monitor consists of long conical gaseous Cherenkov counters that point to the collision region and monitor the average number of inelastic $p\bar{p}$ interactions [20, 21]. The detector consists of two modules which are located in the forward and background region, which covers $3.7 < |\eta| < 4.7$. The total integrated luminosity ($\mathcal{L}$) is derived from the rate of the inelastic $p\bar{p}$ events measured with CLC, $R_{p\bar{p}}$, the CLC acceptance, $\epsilon_{\rm CLC}$, and the inelastic $p\bar{p}$ cross section at 1.96 TeV, σ_{in}, according to the expression,

$$\mathcal{L} = \frac{R_{p\bar{p}}}{\epsilon_{\rm CLC} \cdot \sigma_{in}}.$$

The CLC acceptance, $epsilon_{\rm CLC}$ is 60.2$\pm$2.6%. The inelastic $p\bar{p}$ cross section σ_{in} is 60.7$\pm$2.4 mb. The 5.8% quoted uncertainty is dominated by the uncertainty in the absolute normalization of the CLC acceptance for a single $p\bar{p}$ inelastic collision.

2.2.5 Trigger System

In hadron collider experiments, the trigger system plays an important role. The crossing rate of the Tevatron under 36-on-36 bunch operation is 7.6 MHz, corresponding to 396 ns separation. Since the crossing rate is much higher than the rate at which events can be recorded, the trigger system is designed to select the most interesting physics events. The CDF trigger system has a three level architecture. The block diagram of the trigger system is presented in Figure 10. Level 1 of the trigger system selects events based on information in the calorimeter, tracking chambers and muon detector. The maximum Level 1 event accept rate is roughly 20 kHz, corresponding to an available Level 2 processing time of 50 μsec per event. In Level 2, the cluster finder processes the data collected from Level 1 and from the shower max detectors. And

also Level 2 provides jet reconstruction and secondary vertex information provided by silicon tracker. These events are transformed to Level3 processor farm where the events are reconstructed and filtered with ≤ 50 Hz.

3 Search for fermiophobic Higgs

In the Standard Model, the Higgs boson is introduced to explain the electroweak symmetry breaking (EWSB) and the origin of fermion masses. However, the mechanism for EWSB remains a mystery experimentally. The spontaneous symmetry breaking mechanism requires a single doublet of complex scalar fields. But does Nature follow this minimalistic version or does it require a multi-Higgs sector? The minimal extension of the SM contains an additional Higgs doublet, the "two Higgs doublet model" (2HDM), and the resulting particle spectrum consists of two charged Higgs bosons H^+, H^- and three neutral members h^0, H^0 and A^0. In this model a fermiophobic Higgs boson (h_f) which signifies very suppressed or zero coupling to the fermions, may arise in a paticular version of the 2HDM called type I. In the 2HDM type I one Higgs boublet (Φ_2) couples to all fermion types, while the other doublet (Φ_1) couples. Both doublets couple to the gauge bosons via the kinetic term in the Lagrangian. One vacuum expectation value (v_2) gives masses to all fermion types, while gauge bosons receive masses from both v_1 and v_2. The lightest CP-even Higgs boson h^0 couples to a fermion proportionally to $\cos\alpha/\sin\beta$ (α is mixing angle in the neutral Higgs sector h^0 and H^0) and the h^0 becomes a fermiophobic Higgs when $\alpha = \pi/2$. The β is defined by $\tan\beta = v_2/v_1$.

Fermiophobic Higgs bosons have been searched for at LEP and the Fermilab Tevatron. Combination of results obtained by the LEP collaborations OPAL, DELPHI, ALEPH and L3 yielded a lower bound $m_{h_f} > 109.7$ GeV/c^2. This result was obtained utilizing channel $e^+e^- \to h_f Z, h_f \to \gamma\gamma$.In Run I of the Tevatron the process $qq' \to V^* \to h_f V$, $h_f \to \gamma\gamma$ was used, with the dominant contribution coming from $V = W^\pm$. The limits on m_{h_f} from the CDF and D0 collaborations are, respectively, 78.5 GeV/c^2 and 82 GeV/c^2 at 95% C.L. In Run II The limits on m_{h_f} from the CDF and D0 collaborations are, respectively, 102.5 GeV/c^2 and 106 GeV/c^2 at 95% C.L.

However, all these mass limits assume that the $h_f VV$ coupling is of the same strength as the SM coupling $\phi^0 VV$, which in general would not be the case for a h_f in a realistic model, e.g. the 2HDM (type I). Therefore one could imagine the scenario of a very light h_f ($m_{h_f} \ll 100$ GeV/c^2) which eluded the current searches at LEP and the Tevatron Run I due to suppression in the coupling $h_f VV$. Such h_f could also escape detection in the Tevatron Run II.

In this study we perform a search for 3 γ final states through the process:

$$p\bar{p} \to h_f H^\pm \to h_f h_f W^\pm \to \gamma\gamma\gamma(\gamma) + X.$$

The coupling $H^\pm h_f W^\pm$ is not suppressed if $\tan\beta$ is large.The multi-photon signature has the added virture of very small background rates.

3.1 Models with fermiophobia

A fermiophobic Higgs boson (h_f) may arise in a 2HDM in which one $SU(2) \times U(1)$ Higgs doublet (Φ_2) couples to all fermion types, while the other doublet (Φ_1) does not. Both doublets couple to the gauge bosons via the kinetic term in the Lagrangian. One vacuum expectation value (v_2) gives mass to all fermion types, while gauge bosons receive mass from both v_1 and v_2. This model (usually called "type I") was first proposed in [22]. Due to the mixing in the CP-even neutral Higgs mass matrix (which is diagonalized by α) both CP-even eigenstates h^0 and H^0 can couple to the fermions. The fermionic couplings of the lightest CP-even Higgs boson h^0 take the form

$$h^0 f\bar{f} \sim \frac{\cos\alpha}{\sin\beta}$$

where f is any fermion, and β is defined by $\tan\beta = \dfrac{v_2}{v_1}$.
Small values of $\cos\alpha$ would seriously suppress the fermionic couplings, and in the limit $\cos\alpha \to 0$ the coupling $h^0 f\bar{f}$ would vanish, giving rise to fermiophobia (sometimes called a "bosonic" or "bosophillic" Higgs boson) and the h^0 is called a fermiophobic Higgs(h_f).
The main decay mode of a fermiophobic Higgs boson is $h_f \to \gamma\gamma$. It is the dominant decay for $m_{h_f} \lesssim 95$ GeV, with a BR near 100% for $m_{h_f} \lesssim 80$ GeV, decreasing to 50% at $m_{h_f} \approx 95$ GeV and to 1% at $m_{h_f} \approx 145$ GeV. In contrast, BR($\phi^0 \to \gamma\gamma$) $\approx 0.22\%$ is the largest value in the SM for the two photon decay. We shall be focusing on the possibility of a light ($m_{h_f} \leqslant 100$ GeV) for which the photonic decay mode always has a large BR. BR($h_f \to \gamma\gamma$) is shown in Figure 11.
The conventional production mechanism for a h_f at e^+e^- colliders is $e^+e^- \to Z^* \to h_f Z$, and at hadron colliders $qq' \to V^* \to h_f V$. In the 2HDM (type I), the condition for fermiophobia ($\cos\alpha \to 0$) causes the coupling $h_f VV$ to be suppressed by a factor

$$h_f VV \sim \sin^2(\beta-\alpha) \to \cos^2\beta \equiv \frac{1}{1+\tan^2\beta}.$$

Taking $\tan\beta \geqslant 3(10)$ implies a strong suppression of $\leqslant 0.1(\leqslant 0.01)$ for the coupling $h_f VV$ with respect to the coupling $\phi^0 VV$. This suppression is always possible for the lightest CP-even neutral Higgs boson.Therefore one can imagine the scenario of a very light h_f which eluded the searches via the production process $e^+e^-/qq' \to h_f V$. LEP ruled out regions of the plane $[m_{h_f}, R \times BR(h_f \to \gamma\gamma)]$, where R is defined by

$$R = \frac{\sigma(e^+e^- \to Zh_f)}{\sigma(e^+e^- \to Z\phi^0)}.$$

In a benchmark scenario of $R = 1$, and assuming BR($h_f \to \gamma\gamma$) given by [23, 24], each collaboration derived a limit of around $m_{h_f} \geqslant 100$ GeV, with the combined LEP working group limit being $m_{h_f} \geqslant 109$ GeV. It is trivial to see the necessary suppression in R which would permit a light h_f of a given mass, e.g. $m_{h_f} \geqslant 80$ GeV (50 GeV)

requires $R \leqslant 0.1(0.01)$, which corresponds to $\tan\beta \geqslant 3(10)$ in the 2HDM (type I). Therefore sizable regions of the $[m_{h_f}, R \times BR(h_f \to \gamma\gamma)]$ plane remain unexcluded for small R and small m_{h_f}.In Run I of the Tevatron the process $qq' \to V^* \to h_f V$, $h_f \to \gamma\gamma$ was used, with the dominant contribution coming from $V = W^{\pm}$. The limits on m_{h_f} from and the CDF collaborations are, respectively, 78.5 GeV/c^2 and 82 GeV/c^2 at 95% C.L. In Run II The limits on m_{h_f} from the CDF and D0 collaborations are, respectively, 102.5 GeV/c^2 and 106 GeV/c^2 at 95% C.L.
However, with the expected suppression in the $h_f VV$ coupling ($R < 1$), $m_{h_f} \geqslant 80$ GeV could still escape detection. At the Tevatron Run II, this production process allow discovery of a h_f even in the region where the process $qq' \to W h_f$ is suppressed.

3.2 Production processes

We introduce the production processes which may offer sizable rates for h_f in the region where the coupling $h_f VV$ is very suppressed. These production processes make use of the cascade decays $H^{\pm} \to h_f W^{(*)}$ which may have large BRs in the 2HDM (type I). BR($H^{\pm} \to W h_f$) is shown in Figure 12. These large BRs arise since the coupling of $H^{\pm}$ to all the fermions scales as $1/\tan\beta$, and thus for moderate to large $\tan\beta$ even the three-body decays (i.e. with V^*) can have sizable or dominant BRs.
Below we consider $q\bar{q} \to W^* \to H^{\pm} h_f$. Quark-antiquark annihilation into an intermediate W boson producing a h_f in association with a charged Higgs boson. This process makes use of the Higgs-Higgs-vector boson coupling (g_{HHV}) which is proportional to $\sin\beta$. Production cross section is shown in Figure 13. This $q\bar{q} \to H^{\pm} h_f$ mechanism can offer non-negligible cross sections in the large $\tan\beta$ region. Moreover, double h_f production can occur, resulting in distinctive $\gamma\gamma\gamma(\gamma)$ topologies. In Figure 14 the cross section for $q\bar{q} \to W^* \to H^{\pm} h_f \to h_f h_f W^* \to \gamma\gamma\gamma(\gamma) + X$ is shown. This cross section is given by

$$\sigma(p\bar{p} \to \gamma\gamma\gamma(\gamma) + X) = \sigma(p\bar{p} \to H^{\pm} h_f) \times BR(H^{\pm} \to h_f W^*) \times BR(h_f \to \gamma\gamma)^2.$$

Feynman diagrams of this process is shown below. In this note we will focus on the 3γ event signature as this has very small background rates.

4 Data Samples and Event Selection

In this section we describe the trigger and dataset for preselection of events and the selection of events consist with the 3γ final state. The analysis is based on data collected from run 138425 (February 4, 2002) to run 289197 (February 25, 2010) covering the period 0 though 28, and the corrsponding to integrated luminosity is 6.0 fb^{-1} after run filtering for good detector condition.

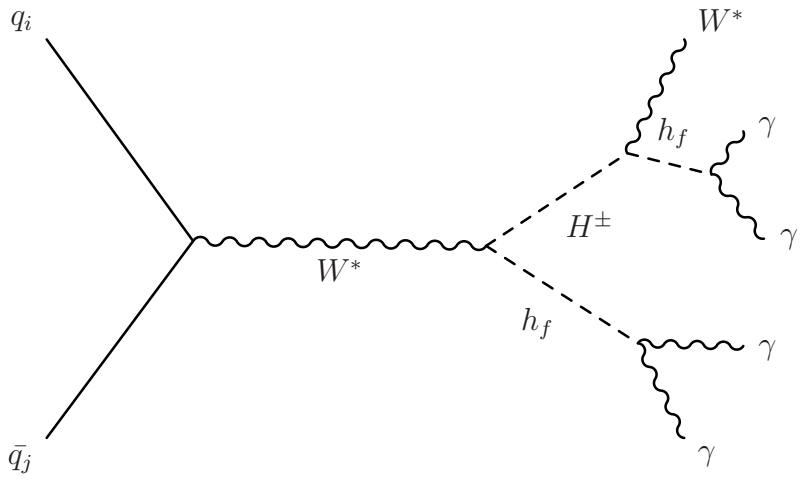

4.1 Triggers and Datasets

The events used in this analysis are required to pass one of the DIPHOTON_12, DIPHOTON_18 or TRIPHOTON triggers. The requirements for each at the three trigger levels are listed in Table 4.

4.2 Event Selection

As described before, the desirable events are 3γ events to search for the fermiophobic Higgs boson (h_f). The 3γ candidate events are selected from the subsample of events that pass one of the triggers. In the sample, 3 photons are requred to pass the standard photon cut. The trigger efficiency is taken to be 100% for these cuts [25]. The standard photon cut is given in Table 5.

5 Signal efficiency

The probability of a 3γ event passing the identification selection must be known in order to predict the expected number of signal events. The efficiency comes from the probability that an event containing 3γ candidates will pass the identification cuts described in Section 4.2. The identification efficiency is measured using Monte Carlo samples.

5.1 Signal Monte Carlo samples

The efficiency is presented as a function of h_f mass for $H^\pm h_f \rightarrow 3\gamma + X$ events, generated using Pythia Monte Carlo, with 40000 events for each h_f mass point in the range 30 GeV/c^2 to 105 GeV/c^2, at an increment of 15 GeV/c^2. The samples are also generated for three cases of $H^\pm$ mass = 90, 120, 150 GeV/c^2. The model of this study is 2HDM (typeI) with fermiophobia and this analysis will cover the region of large

$\tan\beta$. To simulate $p\bar{p} \to H^{\pm}h_f \to 3\gamma + X$, we set $\alpha = \pi/2$ and $\tan\beta = 10$. And H^0 mass is set to 110 GeV/c^2,A^0 mass is set to 120 GeV/c^2.

5.2 Detector Efficiency

We estimate the efficiency by the following simple fraction:

$$\epsilon = \frac{\text{the number of } 3\gamma \text{ events passing the ID cuts}}{\text{the number of events before the ID cuts}}$$

where "the number of 3γ events passing the ID cuts" is to pick out events which include 3 objects passing the standard photon cut described in Section 4.2.
In the region of searching h_f described in Section 5.1, we estimate the efficiency of detecting h_f at CDF as a function of h_f mass Table 6 and Figure 15 show the signal efficiency for each $H^{\pm}$ mass.
The efficiency for each $H^{\pm}$ mass is $5 \sim 8\%$, then rise to $11 \sim 15\%$. As the M_{h_f} become high mass, the efficiency also increases.

6 Background Estimation

There are two major sources of the background events. The first comes from the events in which jets are misidentified as photons. The other source comes from Direct Triphoton Production (DTP), i.e. Direct Diphoton Production along with the FSR/ISR photon. The contribution of fake events arising from detector noise is estimated to be negligible.

6.1 Background With Misidentified Photons

QCD backgrounds to the 3γ+X final state come from direct (fragmentation) photons and/or EM-like jets (denoted by j). They come from the four possible combinations of jets and photons: $\{j,\ j,\ j\}$, $\{j,\ j,\ \gamma\}$, $\{j,\ \gamma,\ \gamma\}$ and $\{\gamma,\ \gamma,\ \gamma\}$. The last component can, in principle, contain the Higgs signal. The number of 3γ events that are produced can be obtained by solving four linear equations: $\vec{\boldsymbol{n}} = \hat{\boldsymbol{E}} \cdot \vec{\boldsymbol{N}}$, where $\vec{\boldsymbol{n}} = (n_{ppp},\ n_{fpp},\ n_{ffp},\ n_{fff})$ denotes a vector of observed events (p =pass, f =fail photon selection) and $\vec{\boldsymbol{N}} = (N_{\gamma\gamma\gamma},\ N_{j\gamma\gamma},\ N_{jj\gamma},\ N_{jjj})$ denotes produced events. And $\hat{\boldsymbol{E}}$ is a 4×4 efficiency matrix:

$$\begin{pmatrix} \epsilon_s^3 & \epsilon_s^2\epsilon_b & \epsilon_s\epsilon_b^2 & \epsilon_b^3 \\ 3(1-\epsilon_s)\epsilon_s^2 & \epsilon_s^2(1-\epsilon_b) + 2(1-\epsilon_s)\epsilon_s\epsilon_b & \epsilon_b^2(1-\epsilon_s) + 2(1-\epsilon_b)\epsilon_b\epsilon_s & 3(1-\epsilon_b)\epsilon_b^2 \\ 3(1-\epsilon_s)^2\epsilon_s & \epsilon_b(1-\epsilon_s)^2 + 2(1-\epsilon_s)(1-\epsilon_b)\epsilon_s & \epsilon_s(1-\epsilon_b)^2 + 2(1-\epsilon_b)(1-\epsilon_s)\epsilon_b & 3(1-\epsilon_b)^2\epsilon_b \\ (1-\epsilon_s)^3 & (1-\epsilon_s)^2(1-\epsilon_b) & (1-\epsilon_s)(1-\epsilon_b)^2 & (1-\epsilon_b)^3 \end{pmatrix}$$

Here the signal and background efficiencies ($\epsilon_s,\ \epsilon_b$) are the probability of a photon and jet to pass photon selection.
The solution of four linear equations gives us the number of events that are produced in the collisions ($\vec{\boldsymbol{N}}$) using the number of observed events ($\vec{\boldsymbol{n}}$). Thus the QCD contribution from $\{j,\ j,\ j\}$, $\{j,\ j,\ \gamma\}$ and $\{j,\ \gamma,\ \gamma\}$ processes is estimated.

6.1.1 ϵ_s, ϵ_b in the efficiency matrix ($\hat{E}$)

We estimate the rate at which a jet originating from a quark or a gluon fakes an isolated photon in the central calorimeter (CEM) to apply as the ϵ_b in the efficiency matrix ($\hat{\boldsymbol{E}}$). We call any photon that is due the decay of a meson (e.g. π^0, η^0) as "fake photons", whereas prompt photons via direct production or radiated off a final state quark make up the "real photon" signal. Our analysis technique follows the one as described in [26].

Our analysis starts by measuring the jet-to-photon fake rate for isolated jets from a sample of jet-triggered events. Utilizing the entire jet sample reduces statistical uncertainties by making use of a large sample of jets and possesses the added benefit of allowing estimations of systematic errors in the fake rate from different jet selections. This fake rate is refered to as $P_{raw}(\mathrm{E}_T)$. The "raw" means that the selected "jet" are a combination of hadronic quark/gluon showers and direct photons. The detailed selection jets and the measurement of P_{raw} is described in the Appendix A. The correction must be made to $P_{raw}(\mathrm{E}_T)$ to obtain the "true" fake rate $P_{true}(\mathrm{E}_T)$ that is applied to ϵ_b in efficiency matrix ($\hat{\boldsymbol{E}}$). We detail the measurement of the correction in the Appendix A.

1. The $P_{raw}(\mathrm{E}_T)$ is the fraction of jets which pass the standard photon cut in Section 4.2. We require E_T cut to be $\mathrm{E}_T > 15$ GeV as reference. The $P_{raw}(\mathrm{E}_T)$ represents an upper limit on the actual fake rate since it is contaminated by true photons N_γ^{true}.

$$P_{raw} = \frac{N_{\gamma-candidate}}{N^{jet}} = \frac{N_\gamma^{true} + N_{jet\to\gamma}}{N^{jet}}$$

2. The $P_{raw}(\mathrm{E}_T)$ must be corrected for the fraction of the accepted "jet" that are true hadronic quark/gluon showers and not a contamination from real photons. This correction factor is referred to as F_{QCD}:

$$F_{QCD} = \frac{N_{jet\to\gamma}}{N_{\gamma-candidate}} = \frac{N_{jet\to\gamma}}{N_\gamma^{true} + N_{jet\to\gamma}}$$

   We used the Isolation vs CES χ^2 method to determine the prompt photon fraction (F_{QCD}) [26].

3. We correct the raw fake rate by the "true" photon contamination to obtain the true fake rate. The true fake rate ($P_{true}(\mathrm{E}_T)$) is obtained by multiplying the raw fake rate ($P_{raw}(\mathrm{E}_T)$) with the F_{QCD}.

$$P_{true} = \frac{N_{jet\to\gamma}}{N^{jet}} = \frac{N_{\gamma-candidate}}{N^{jet}} \times \frac{N_{jet\to\gamma}}{N_{\gamma-candidate}} = P_{raw} \times F_{QCD}$$

Figure 16 shows $P_{true}(\mathrm{E}_T)$ outlined above.

We estimate the probability of a photon to pass photon selection. The process $Z \rightarrow ee$ is used to define a pure sample of electrons. Because a pure sample of photons from detector data is unavailable, the probability is calculated using efficiencies for electrons from the detector. It is assumed that electrons and photons behave similarly in the detector. Our analysis technique follows the one as described in [27]. We detail the measurement of the probability in Appendix B. We use the probability of a photon to pass the standard photon cut in Section 4.2 as ϵ_s in the efficiency matrix ($\hat{E}$). Table 7 display ϵ_s for the sets of data, with a statistical error added.

6.1.2 Calculation of fake event

The numbers of events observed $\vec{\boldsymbol{n}}$ have the objects passing or failing the standard photon cut in Section 4.2. We use jet objects or EM objects as the failed objects. Jet objects with $\mathrm{E}_T > 15$ GeV and $|\eta| < 1.1$ are considered for the central photon backgrounds. EM objects are required to pass at least CEM, CES fiduciality cuts and not to have associated track (i.e. to pass the cuts of associated track). But this EM objects are required to fail the standard photon cut. Thus n_{ppp} is the number of observed events which have 3 objects passing standard photon cut, n_{fpp} is the number of observed events which have 2 objects passing standard photon cut and 1 jet or EM object described above and the same can be said for n_{ffp} and n_{fff}.
The efficiency matrix ($\hat{E}$) include ϵ_b which is the E_T dependent probability of a jet faking a photon. The elements of $\hat{E}$ also depend on E_T and we make $\hat{E}$ for each E_T when we solve four linear equations:$\vec{\boldsymbol{n}} = \hat{\boldsymbol{E}} \cdot \vec{\boldsymbol{N}}$.
The number of events that are produced in the collisions ($\vec{\boldsymbol{N}}$) are obtained by solving the above equation. The number of the QCD contribution ($n^{3\gamma}_{fake}$) from $\{j,\ j,\ j\}$, $\{j,\ j,\ \gamma\}$ and $\{j,\ \gamma,\ \gamma\}$ is estimated by the following equation.

$$n^{3\gamma}_{fake} = \epsilon_s^2\epsilon_b \times N_{jj\gamma\gamma} + \epsilon_s\epsilon_b^2 \times N_{jjj\gamma} + \epsilon_b^3 \times N_{jjj}$$

Thus the background that comes from events with at least on misidentified photon is estimated to be

$$n^{3\gamma}_{fake} = 5.1 \pm 1.1 \text{ events (stat. only)}.$$

The systematic uncertainty on the number of fake events include the uncertainty on the photon ID efficiency and the uncertainty of jet-to-photon fake rate due to jet selection differences among jet samples.
We take a systematic uncertainty of 2.7% for the photon ID per photon as described in [27]. The contribution of these systematic uncertainties to fake event is 2%.
The systematic uncertainty from fake rate is 10%. The dominant uncertainty in the fake event is the systematic uncertainty on the fake rate To get the systematic uncertainty on the fake rates we use the uncertainties of Figure 16.

6.2 Direct Tri-Photon Background

We estimate the DTP background in the following way. We scale the corrected number of di-photon events observed in data ($N^{\gamma\gamma}(Data)$) with the rate at which one would expect to observe a third photon in Direct Di-photon Production (DDP) processes from PYTHIA:

$$n^{3\gamma}_{DTP} = \frac{N_{\gamma\gamma\gamma}(MC)}{N_{\gamma\gamma}(MC)} \cdot N^{\gamma\gamma}(Data) \cdot \rho$$

Here, because the di-photon data sample contains a non-negligible fraction of $\gamma + j$ and $j + j$ events, we apply a purity factor, $\rho = n^{2\gamma}_{DDP}/(n^{2\gamma}_{DDP} + n^{2\gamma}_{\gamma+j} + n^{2\gamma}_{j+j})$. For simulating di-photon, we use gexo1g data set, which is di-photon PYTHIA filtered for at least $E_T > 10$ and $|\eta| < 3$ two photons with pile-up vertices.

6.2.1 Purity factor ρ

We extract ρ from data using a matrix method similar to the one employed in the Section 6.1. This time, however, we compose a 3×3 efficiency matrix:

$$\begin{pmatrix} \epsilon_s^2 & \epsilon_s\epsilon_b & \epsilon_b^2 \\ 2(1-\epsilon_s)\epsilon_s & \epsilon_s(1-\epsilon_b) + (1-\epsilon_s)\epsilon_b & 2(1-\epsilon_b)\epsilon_b \\ (1-\epsilon_s)^2 & (1-\epsilon_s)(1-\epsilon_b) & (1-\epsilon_b)^2 \end{pmatrix}$$

and relate contributions from $\{\gamma, \gamma\}$, $\{\gamma, j\}$, and $\{j, j\}$ processes to the $n_{i,j}$ numbers of observed two-body events. Here, indices i and j can be p or f, and as before, $p(f)$ indicates — "passed(failed) the standard photon cuts". The number of observed events that pass/fail photon cuts is given by $\vec{\boldsymbol{n}} = (n_{pp}, n_{pf}, n_{ff})$. The rates in the efficiency matrix (ϵ_s, ϵ_b) are the probability of a photon to pass photon selection and jet-to-photon fake rate obtained in Section 6.1.1.
Thus we proceed with solving for the number of produced events: $\vec{\boldsymbol{N}} = (N_{\gamma\gamma}, N_{j\gamma}, N_{jj})$. This gives individual contributions to the observed di-photon final state:

$$(n^{2\gamma}_{DDP},\ n^{2\gamma}_{\gamma+j},\ n^{2\gamma}_{j+j}) = (\epsilon_s^2 \times N_{\gamma\gamma},\ \epsilon_s\epsilon_b \times N_{j\gamma},\ \epsilon_b^2 \times N_{jj}),$$

resulting in purity $\rho = n^{2\gamma}_{DDP}/(n^{2\gamma}_{DDP} + n^{2\gamma}_{\gamma+j} + n^{2\gamma}_{j+j})$ in Table 8, with a statistical error added.

6.2.2 Calculation of DTP event

PYTHIA MC of DDP, DTP events and data of DDP give the estimated DTP background as:

$$n^{3\gamma}_{DTP} = 3.4 \pm 0.4 \text{ events (stat. only)}.$$

The systematic uncertainty on the number of DTP events include the uncertainty from the photon ID efficiency, jet-to-photon fake rate, PDF, ISR/FSR, Q^2 (renormalization scale) uncertainties. We obtain the systematic uncertainies from the photon

ID efficiency and jet-to-photn fake rate in a similar way of fake event. The systematic uncertainty from the photon ID efficiency is 2.6% and the uncertainty on the jet-to-photon fake rate is 12%.
For the systematic uncertainties from PDF, ISR/FSR, Q^2 uncertainties we follow the standard procedure at CDF. The systematic uncertainty from PDF is 1.5%, the uncertainty from ISR/FSR is 23%, and the uncertainty from Q^2 is 13%. The dominant uncertainty in the DTP event is the systematic uncertainty on ISR/FSR.

6.3 Background Summary

The total background to the 3γ+X final state is estimated to be the sum of $n^{3\gamma}_{fake} = 5.1$ events and $n^{3\gamma}_{DTP} = 3.4$ events. Table 9 shows the estimated total background events with statistical and systematic errors.
After condidering all the backgrounds, the expected E_T distributions, for all combined backgrounds of fake event and DTP event are shown in Figure 17.

7 Side-band event

The typical CDF analysis proceeds, before unbliding the results according to the search algorithm, to test the algorithm. We therefore perform cross-check to justify our analysis algorithms.
We compare the side-band event between data and our expectations. We define the side-band event as $2\gamma + 1$ loose γ event that has two objects to pass the standard photon selection and one object to fail the standard photon selection but pass loose photon selection.

7.1 Loose γ

A Loose photon is required to pass the loose photon cut but fail standard photon cut of Table 5. The loose photon cut is given in Table 10. The differences between the standard photon cut and the loose photon cut are E_{Had}/E_{EM}, Iso E_T, Track P_T, and Track Iso. χ^2(Strips+Wires)/2.0 and 2^{nd} CES cluster cut are removed. Regarding the loose photon cut, we refer [28] as with the standard photon cut.

7.2 Fake event in side-band

We estimate the fake events in side-band using the same way in the Section 6.1. For $2\gamma + 1$ loose γ event, the 4×4 efficiency matrix $\hat{\boldsymbol{E}}$ is changed to $\hat{\boldsymbol{E}}_l$:

$$\begin{pmatrix} 3\epsilon_s^2(1-\epsilon_s)\epsilon_{s_l} & \epsilon_s^2\epsilon_{b_l} + 2(1-\epsilon_s)\epsilon_{s_l}\epsilon_s\epsilon_b & (1-\epsilon_s)\epsilon_{s_l}\epsilon_b^2 + 2\epsilon_s\epsilon_{b_l}\epsilon_b & 3\epsilon_b^2\epsilon_{b_l} \\ 3(1-\epsilon_s)\epsilon_s^2 & \epsilon_s^2(1-\epsilon_b) + 2(1-\epsilon_s)\epsilon_s\epsilon_b & \epsilon_b^2(1-\epsilon_s) + 2(1-\epsilon_b)\epsilon_b\epsilon_s & 3(1-\epsilon_b)\epsilon_b^2 \\ 3(1-\epsilon_s)^2\epsilon_s & \epsilon_b(1-\epsilon_s)^2 + 2(1-\epsilon_s)(1-\epsilon_b)\epsilon_s & \epsilon_s(1-\epsilon_b)^2 + 2(1-\epsilon_b)(1-\epsilon_s)\epsilon_b & 3(1-\epsilon_b)^2\epsilon_b \\ (1-\epsilon_s)^3 & (1-\epsilon_s)^2(1-\epsilon_b) & (1-\epsilon_s)(1-\epsilon_b)^2 & (1-\epsilon_b)^3 \end{pmatrix}$$

We obtain ϵ_s, ϵ_b in Section 6.1.1. The probability of a photon to pass loose photon ID cuts is ϵ_{s_l} and the jet-to-loose photon fake rate is ϵ_{b_l}. Table 11 shows ϵ_{s_l} and Figure 18 shows ϵ_{b_l}. We detail ϵ_{s_l} in Appendix B and ϵ_{b_l} in Appendix A. The number of events that are produced in the collisions ($\vec{\boldsymbol{N}}_l$) are obtained by solving four linear equations: $\vec{\boldsymbol{n}}_l = \hat{\boldsymbol{E}}_l \cdot \vec{\boldsymbol{N}}_l$, where $\vec{\boldsymbol{n}}_l = (n_{ppp_l},\ n_{fpp},\ n_{ffp},\ n_{fff})$ denotes a vector of observed events (p =pass, f =fail photon selection, and p_l =pass loose photon selection) and $\vec{\boldsymbol{N}}_l = (N_{\gamma\gamma\gamma},\ N_{j\gamma\gamma},\ N_{jj\gamma},\ N_{jjj})$ denotes produced events.
The number of the QCD contribution (n^{SB}_{fake}) in side-band from $\{j,\ j,\ j\}$, $\{j,\ j,\ \gamma\}$ and $\{j,\ \gamma,\ \gamma\}$ is estimated by the following equations.

$$\begin{aligned} n^{SB}_{fake} &= E^{1,2}_l \times N_{j\gamma\gamma} + E^{1,3}_l \times N_{jj\gamma} + E^{1,4}_l \times N_{jjj} \\ E^{1,2}_l &= \epsilon_s^2\epsilon_{b_l} + 2(1-\epsilon_s)\epsilon_{s_l}\epsilon_s\epsilon_b \\ E^{1,3}_l &= (1-\epsilon_s)\epsilon_{s_l}\epsilon_b^2 + 2\epsilon_s\epsilon_{b_l}\epsilon_b \\ E^{1,4}_l &= 3\epsilon_b^2\epsilon_{b_l} \end{aligned}$$

Thus the misidentified photon events in side-band are estimated to be

$$n^{SB}_{fake} = 14.5 \pm 2.6 \text{ events (stat. only)}.$$

The systematic uncertainty from the photon ID efficiency is 2% and the uncertainty from the jet-to-photon fake rate is 5% in side-band.

7.3 DTP event in side-band

We estimate the DTP events in side-band using the same way in the Section 6.2. The number of DTP events in side-band is estimated by the following equation.

$$\begin{aligned} n^{SB}_{DTP} &= \frac{N_{\gamma\gamma\text{loose}}(MC)}{N_{\gamma\gamma}(MC)} \cdot N^{\gamma\gamma}(Data) \cdot \rho \\ \rho &= \frac{n^{2\gamma}_{DDP}}{n^{2\gamma}_{DDP} + n^{2\gamma}_{\gamma+j} + n^{2\gamma}_{j+j}} \end{aligned}$$

$N_{\gamma\gamma\gamma}$(MC) is changed to $N_{\gamma\gamma\text{loose}}$(MC) for side-band event in these equations compared with Section 6.2. These equations give the estimated DTP events in side-band as:

$$n^{SB}_{DTP} = 1.2 \pm 0.3 \text{ events (stat. only)}.$$

The systematic uncertainties from the photon ID efficiency, jet-to-photon fake rate, PDF, ISR/FSR, and Q^2 are 4.0%, 22%, 2.0%, 38%, and 19%.

7.4 Summary of side-band event

The Number of total events in side-band is estimated to be the sum of $n^{SB}_{fake} = 14.5$ events and $n^{SB}_{DTP} = 1.2$ events. Table 12 shows the estimated total side-band events with statistical and systematic errors.
The expected E_T distributions, for all combined events are shown in Figure 19 with data. Our expectation and observation of side-band event agree well.

8 Estimation of the Systematic Uncertainties

We define the sensitivity of the search to be equal to the expected 95% C.L. cross section limits. In order to calculate them, we need to estimate the uncertainties for the trigger, luminosity, background and detector efficiency. As mentioned in Section 4, with our combination of triggers and high E_T photons we take a trigger efficiency of 100% with negligible error [25]. The systematic unertainty on the luminosity is taken to be 6% with major contributions from the uncertainties on the CLC efficiency and from the precision of the detector simulation and the event generator [29]. The systematic uncertainty on the background in the signal region is determined from our understanding of both fake event and DTP event, as described in Section 6. The systematic uncertainty on the detector efficiency is estimated in the subsections below. The results are summarized in Table 13 for an example mass of $h_f = 50$ GeV and $H^{\pm} = 90$ GeV. We take the systematic uncertainty to be constant for all masses.

8.1 Uncertainties of Detector Efficiency

There are a number of effects that can cause our estimate of the detector efficiency to be systematically mis-estimated. We identify them here and explain how they are estimated. The dominant uncertainty on the efficiency is the photon ID.

8.1.1 Photon ID

The photon ID variables are imperfectly modeled in *cdfSim*. This has been studied in detail elsewhere. We take a systematic uncertainty of 2.7% per photon, as described in [27]. Since there are three photons we take the total systematic uncertainty to be $3 \times 2.7\% = 8.1\%$.

8.1.2 PDF

In an event where proton and antiproton bunches collide it is mostly a single subparticle of the (anti-)proton, a parton (quark or gluon), that participates in the hard collision and produces a high center-of-mass energy event. The momentum fraction, described by parton distribution function (PDF), that is carried by each of the partons in the proton or anti-proton is not perfectly understood. It affects the kinematics of the outgoing final state particles. To estimate the magnitude of this effect on the detector efficiency we use the standard technique of evaluating the uncertainty, event-by-event, on the momentum fraction of the colliding parton using a standardized "PDF-set" by the `CTEQ` collaboration (`CTEQ-5L`) [30]. As only the newer PDF-set version `CTEQ-6M` contains 90% confidence intervals for each eigenvector, the total uncertainty is estimated using a standard procedure by reweighting the parton momenta of the original `CTEQ-5L` set and varying the PDFs using the uncertainties from `CTEQ-6M` as described in [30]. We get a relative uncertainty of 1.0% on the detector efficiency.

8.1.3 ISR/FSR (Initial and Final State Radiation

Initial state radiation (ISR) caused by a gluon radiating from an incoming parton or final state radiation (FSR) from an outgoing jet can both make the E_T spectrum of the final state particles softer than expected without radiation. This can cause the photon or the jets to be systematically more or less likely to pass the kinematic requirements. The effect carries a non-negligible theoretical uncertainty and is estimated using the standard CDF procedure as described in [31]. Doing so we find a variation in the detector efficiency, taken to be the systematic uncertainty, of 2.0%.

8.1.4 Q^2 (Renormalization Scale)

We include the systematic uncertainty on the efficiency due to variations in the Q^2 scale. The variation observed by changing the scale from $0.25 \cdot q^2$ to $4 \cdot q^2$ is calculated to be 3.0%.

8.1.5 Summary of the Systematic Uncertainties

All systematic errors are combined in quadrature to give a total systematic uncertainty of 8.9% used in the limit calculation. The individual results are given in Table 13.

9 Optimization and Expected Limits

Now that the background estimation methods are determined and the signal efficiency is available for a given cut, along with their uncertainties, an optimization procedure can be readily employed. Using only simple cut we can conduct a robust search. We can then optimize that cut before unblinding the signal region. We choose to optimize for E_T^1+E_T^2 cut. Let us recall that the underlying signal event has four photons and two jets or a lepton from a W. Each object is quite energetic carrying on average 10-20 GeV of energy in the transverse plane. Thus 3γ (h_f signal) has lots of E_T^1+E_T^2 compared to SM backgrounds, which are dominated by fake and DTP backgrounds which do not have lots of high E_T objects.
Figure 20 shows the distributions of E_T normalized to the number of expected events. Figure 21 shows the distribution of E_T^1+E_T^2 for 3γ events. We compare the background distribution before unbliding the signal region and the expected signal in the signal region for an example mass of $h_f = 75$ GeV and mass of $H^{\pm} = 120$ GeV.

By estimating our sensitivity using 95% C.L. expected cross section limits, in the no-signal assumption, we find an optimal cut before unblinding the signal region. We use the Bayesian limit calculation [32] to calculate the limits, taking into account the predicted number of background events, the efficiency, the luminosity and their systematic uncertainties. The predicted number of background events and the efficiency are a function of the cut choices, so the expected cross section limit is also just a function

of the cut ($55 \leq E_T^1+E_T^2 \leq 125$ in steps of 10). For each mass of h_f and mass of $H^\pm$ combination the minimum expected cross section limit defines our optimal cut. The exclusion region is defined by the region where the theoretical cross section is above the 95% C.L. cross section limit. For an example of $E_T^1+E_T^2 > 55$ Figure 22 shows the theoretical cross section and the 95% C.L. cross section limit. In this case the exclude region is $m_{h_f} < 72$ GeV for the mass of $H^\pm = 90$ GeV. We choose the $E_T^1+E_T^2$ cut to make the exclude region wide. Figure 23 shows the h_f mass limit for each mass of $H^\pm$. This figures show the excluded region of h_f mass. We choose $E_T^1+E_T^2 > 95$ GeV as this cut maximizes and stabilizes the mass limit.

With this cut we predict 1.9 ± 0.9 backround events with 0.5 ± 0.3 from fake event and 1.4 ± 0.9 from DTP event. These backround events are calculated after the optimal cuts. Table 14 and 15 show the background events and efficiency for the final selection requirement. Table 16 shows the expected cross section limits and theoretical cross section of each m_{h_f} and $m_{H^\pm}$. Figure 24 shows the expected 95% C.L. cross section limit and theoretical cross section for $E_T^1+E_T^2 > 95$ for each $H^\pm$ mass.

To check our algorithm of backround estimation we compare data with the expectations in $E_T^1+E_T^2 < 75$. Figure 25 show the expected E_T distributions in $E_T^1+E_T^2 < 75$. Table 17 shows the number of total events in $E_T^1+E_T^2 < 75$. Our expectation and observation in $E_T^1+E_T^2 < 75$ also agree well.

10 Conclusion

As described above sections, there is no significance discrepancies between data and background expectation for number of events in $E_T^1+E_T^2 > 95$ of 3γ events (Table 14). In this section we can show the exclusion regions as a function of m_{h_f} for each $m_{H^\pm}$ using the expected cross section limits as described in Section 9. The results from the expected and observed cross section limits shown in Figure 26 represent the excluded region for a fermiophobic Higgs boson in the class of Two Higgs Doublets Models.
The exclusion regions is as follows:

- $m_{h_f} \leq 74.6$ GeV/c^2 for $m_{H^\pm} = 90$ GeV/c^2
- $m_{h_f} \leq 88.0$ GeV/c^2 for $m_{H^\pm} = 120$ GeV/c^2
- $m_{h_f} \leq 78.2$ GeV/c^2 for $m_{H^\pm} = 150$ GeV/c^2

Table 1: List of the leptons and quarks and its properties in the Standard Model [1].

Name	Symbol	Mass		Charge ($Q/\|e\|$)	Spin	Weak Isospin
		Leptons				
electron	e	0.509	MeV/c^2	-1	1/2	$+1/2$
electron neutrino	ν_e	<225(95%CL)	eV/c^2	0	1/2	$-1/2$
muon	μ	105.7	MeV/c^2	-1	1/2	$+1/2$
muon neutrino	ν_μ	<0.19(90%CL)	MeV/c^2	0	1/2	$-1/2$
tau	τ	1776.8	MeV/c^2	-1	1/2	$+1/2$
tau neutrino	ν_τ	<18.2(95%CL)	MeV/c^2	0	1/2	$-1/2$
		Quarks				
up	u	$2.55^{+0.75}_{-1.05}$	MeV/c^2	$+2/3$	1/2	$+1/2$
down	d	$5.04^{+0.96}_{-1.54}$	MeV/c^2	$-1/3$	1/2	$-1/2$
charm	c	$1.27^{+0.07}_{-0.11}$	GeV/c^2	$+2/3$	1/2	$+1/2$
strange	s	104^{+26}_{-34}	MeV/c^2	$-1/3$	1/2	$-1/2$
top	t	171.2 ± 2.1	GeV/c^2	$+2/3$	1/2	$+1/2$
bottm	b	$4.20^{+0.17}_{-0.07}$	GeV/c^2	$-1/3$	1/2	$-1/2$

Table 2: Summry of the forces and gauge bosons in the Standard Model.

Interaction	Gauge boson (symbol)	Mass (GeV/c^2)	Effective coupling	Range [cm]	Typical time [s]
Electromagnetic	photon (γ)	0	1/137	∞	10^{-20}
Weak	$W^\pm$, Z^0	80.4, 91.2	10^{-5}	10^{-16}	10^{-10}
Strong	gluon (g)	0	~ 1	10^{-13}	10^{-23}

Table 3: The neutral Higgs boson couplings to gauge bosons ($V = W^{\pm}, Z$) and fermions in 2HDM Type-I.

ϕ	H^0	h^0	A^0
$g_{\phi VV}$	$\cos(\beta-\alpha)$	$\sin(\beta-\alpha)$	0
$g_{\phi\bar{u}u}$	$\frac{\sin\alpha}{\sin\beta}$	$\frac{\cos\alpha}{\sin\beta}$	$\cot\beta$
$g_{\phi\bar{d}d}$	$\frac{\sin\alpha}{\sin\beta}$	$\frac{\cos\alpha}{\sin\beta}$	$\cot\beta$
$g_{\phi\bar{e}e}$	$\frac{\sin\alpha}{\sin\beta}$	$\frac{\cos\alpha}{\sin\beta}$	$\cot\beta$

Table 4: Trigger selection

DIPHOTON_12	
L1	Single tower $E_T > 8$ GeV
	Single tower Had/EM< 0.125 unless $E_T > 14$ GeV
L2	Two high E_T pass clusters, $E_T > 10$ GeV, $\|\eta\| < 3.6$
	Both clusters Had/EM< 0.125
	Both clusters Iso< 3 || Iso$< 0.15E_T$
L3	Two L3 clusters, $E_T > 12$ GeV
	Both clusters Had/EM$< 0.055 + 0.00045$E || $E_T > 200$ GeV
	Both clusters Iso(cone 0.4)< 2 || $< 0.10E_T$
	for central, average and scaled CES $\chi^2 < 20$
DIPHOTON_18	
L1	Single tower $E_T > 8$ GeV
	Single tower Had/EM< 0.125 unless $E_T > 14$ GeV
L2	Two high E_T pass clusters, $E_T > 16$ GeV, $\|\eta\| < 3.6$
	Both clusters Had/EM< 0.125
L3	Two L3 clusters, $E_T > 18$ GeV
	Both clusters Had/EM$< 0.055 + 0.00045$E || $E_T > 200$ GeV
	for central, average and scaled CES $\chi^2 < 20$
TRIPHOTON	
L1	Single tower $E_T > 8$ GeV
	Single tower Had/EM< 0.125 unless $E_T > 14$ GeV
L2	Three high E_T pass clusters, $E_T > 10$ GeV, $\|\eta\| < 3.6$
	Clusters Had/EM< 0.125
L3	Three L3 clusters, $E_T > 10$ GeV

Table 5: Summary of the photon ID cuts

Standard Photon Cut	
detector	CEM
$E_T > 15$	
CES fiduciality	
$\lvert X_{CES}\rvert \leq 21$cm, 9cm$\leq \lvert Z_{CES}\rvert \leq$230cm	
E_{Had}/E_{EM}	
$\leq 0.055 + 0.00045\times E$ or ≤ 0.125	
corrected cone 0.4 Iso E_T	
$E_T \leq 20$	$\leq 0.1\times E_T$
$E_T > 20$	$\leq 2.0 + 0.02 \times (E_T - 20)$
χ^2(Strips+Wires)/2.0 < 20	
N3D tracks in cluster ≤ 1	
Track $P_T \leq 1.0 + 0.005\times E_T$ (N3D=1)	
Cone 0.4 Track Iso $\leq 2.0 + 0.005\times E_T$	
E_T of 2^{nd} CES cluster (wire and strip)	
$E_T < 18$ GeV	$\leq 0.14\times E_T$
$E_T \geq 18$ GeV	$\leq 2.4 + 0.01 \times (E_T - 20)$

Table 6: Detector efficiencies for $H^{\pm} = 90,\ 120,\ 150$ GeV/c^2, measured using simulation, showing statistical errors only.

h_f mass(GeV/c^2)	30	40	45	50	60	70	77
Efficiency	0.050	0.072	0.081	0.088	0.100	0.106	0.112
($M_{H^{\pm}}$=90 GeV/c^2)	±0.001	±0.001	±0.001	±0.002	±0.002	±0.002	±0.002

h_f mass(GeV/c^2)	30	45	60	75	90	100
Efficiency	0.051	0.088	0.115	0.121	0.130	0.131
($M_{H^{\pm}}$=120 GeV/c^2)	±0.001	±0.002	±0.002	±0.002	±0.002	±0.002

h_f mass(GeV/c^2)	30	45	60	75	90	105
Efficiency	0.077	0.099	0.109	0.127	0.137	0.146
($M_{H^{\pm}}$=150 GeV/c^2)	±0.001	±0.002	±0.002	±0.002	±0.002	±0.002

Table 7: The probability of a photon to pass photon selection (ϵ_s). We use the probability as ϵ_s in the efficiency matrix ($\hat{E}$) when calculating fake event. We also use ϵ_s when we obtain the purity factor in DTP event.

Periods	0-9	10-17	18-28
ϵ_s (%)	87.1±1.1	84.0±1.1	80.9±0.8

Table 8: Purity factor ρ. We obtain the rate of Direct Di-photon Production events in Di-photon events that have two photons through standard photon selection.

Periods / E_T (GeV)	0-9	10-17	18-28
15-16	0.72±0.03	0.79±0.03	0.81±0.02
16-17	0.76±0.03	0.83±0.03	0.85±0.02
17-18	0.77±0.03	0.84±0.03	0.86±0.03
18-19	0.82±0.03	0.85±0.03	0.87±0.03
19-20	0.81±0.03	0.86±0.03	0.89±0.03
20-140	0.81±0.01	0.85±0.01	0.86±0.01
140-200	0.86±0.33	0.88±0.33	0.91±0.23

Table 9: Total background to the 3γ+X final state

	Events	Statistical error (events)	Systematic error (events)
fake	5.1	1.1	0.5
DTP	3.4	0.4	1.0
Total	8.5	1.1	1.1

Table 10: Summary of the loose photon ID cuts

Loose Photon Cut	
detector	CEM
$E_T > 15$	
CES fiduciality $\lvert X_{CES}\rvert \leq 21$cm, 9cm$\leq \lvert Z_{CES}\rvert \leq$230cm	
E_{Had}/E_{EM} ≤ 0.125	
corrected cone 0.4 Iso E_T	
$E_T \leq 20$	$\leq 0.15 \times E_T$
$E_T > 20$	$\leq 3.0 + 0.02 \times (E_T - 20)$
N3D tracks in cluster ≤ 1	
Track $P_T \leq 0.25 \times E_T$ (N3D=1)	
Cone 0.4 Track Iso ≤ 5.0	

Table 11: The probability of a photon to pass loose photon selection (ϵ_{s_l}). We use the probability as ϵ_{s_l} in the efficiency matrix ($\hat{\boldsymbol{E}}_l$) when calculating fake event in side-band.

Periods	0-9	10-17	18-28
ϵ_s (%)	90.2±1.1	87.2±1.1	85.2±0.8

Table 12: Total side-band event and data

	Events	Statistical error (events)	Systematic error (events)
fake	14.6	2.6	0.9
DTP	1.2	0.3	0.6
Total	15.8	2.6	1.1
Data	16		

Table 13: Summary of the systematic uncertainties on the detector efficiency for an example $h_f = 50$ GeV and $H^{\pm} = 90$ GeV. In the limit calculation we get the full limit from taking into account the systematic uncertainties on the efficiency in quadrature to get 8.9% uncertainty.

Factor	Relative Systematic Uncertainty (%)
Photon ID	8.1
PDF	1.0
ISR/FSR	2.0
Q^2	3.0
Total	8.9

Table 14: Background to the 3γ+X final state for the final selection requirement.

	Events	Statistical error (events)	Systematic error (events)
fake	0.5	0.3	0.1
DTP	1.4	0.3	0.8
Total	1.9	0.4	0.8
Data	3		

Table 15: The efficiency for various m_{h_f} and $m_{H^\pm}$ for the final selection requirement.

m_{h_f} (GeV/c^2)	$m_{H^\pm}$ (GeV/c^2)	Efficiency (%)	Statistical error	Systematic error
30	90	2.06	$\pm$0.07	$\pm$0.19
30	120	2.50	$\pm$0.08	$\pm$0.22
30	150	4.81	$\pm$0.11	$\pm$0.45
40	90	3.55	$\pm$0.10	$\pm$0.32
45	90	4.20	$\pm$0.10	$\pm$0.38
45	120	5.33	$\pm$0.12	$\pm$0.48
45	150	6.94	$\pm$0.14	$\pm$0.62
50	90	4.81	$\pm$0.11	$\pm$0.43
60	90	6.45	$\pm$0.13	$\pm$0.58
60	120	8.43	$\pm$0.15	$\pm$0.76
60	150	8.18	$\pm$0.15	$\pm$0.74
70	90	8.08	$\pm$0.15	$\pm$0.73
75	120	10.4	$\pm$0.17	$\pm$0.94
75	150	11.1	$\pm$0.18	$\pm$0.10
77	90	9.36	$\pm$0.16	$\pm$0.84
90	120	12.4	$\pm$0.19	$\pm$1.1
90	150	13.1	$\pm$0.19	$\pm$1.2
100	120	12.9	$\pm$0.19	$\pm$1.2
105	150	14.5	$\pm$0.20	$\pm$1.3

Table 16: The expected cross section limits for various m_{h_f} and $m_{H^\pm}$ for the final selection requirement. The theoretical cross section is σ^{theo}.

m_{h_f} (GeV/c^2)	$m_{H^\pm}$ (GeV/c^2)	σ_{95}^{exp} (fb)	σ^{theo} (fb)
30	90	40.85	242.7
30	120	33.66	84.51
30	150	17.46	36.28
40	90	23.66	177.8
45	90	20.04	151.8
45	120	15.76	61.36
45	150	12.12	27.99
50	90	17.47	128.4
60	90	13.03	83.55
60	120	9.974	41.03
60	150	10.28	19.64
70	90	10.41	33.73
75	120	8.063	22.64
75	150	7.566	11.29
77	90	8.983	5.772
90	120	6.753	7.041
90	150	6.401	3.823
100	120	6.512	0.6569
105	150	5.809	0.5823

Table 17: Background to the 3γ+X final state for $E_T^{1st}+E_T^{2nd} < 75$.

	Events	Statistical error (events)	Systematic error (events)
fake	3.87	0.95	0.44
DTP	1.29	0.28	0.90
Total	5.16	1.00	1.00
Data	3		

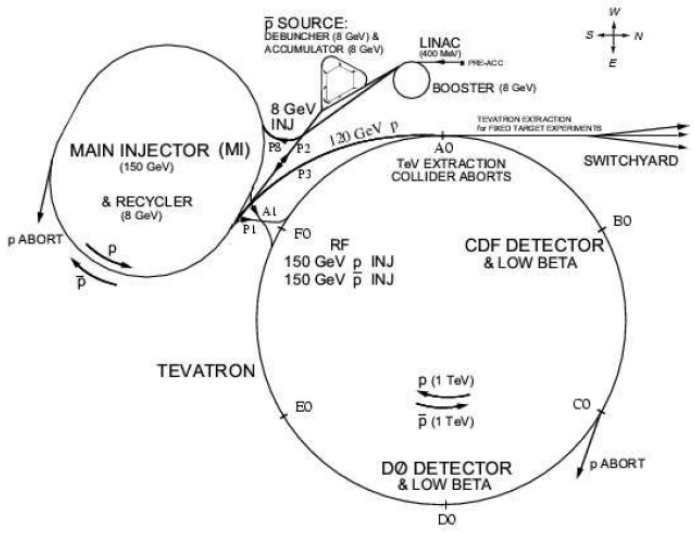

Figure 1: Tevatron Accelerator with a circumference of approximately 4 miles which accelerates protons or antiprotons from 150 GeV to 980 GeV. The protons and antiprotons share the same ring. The protons travel clockwise.

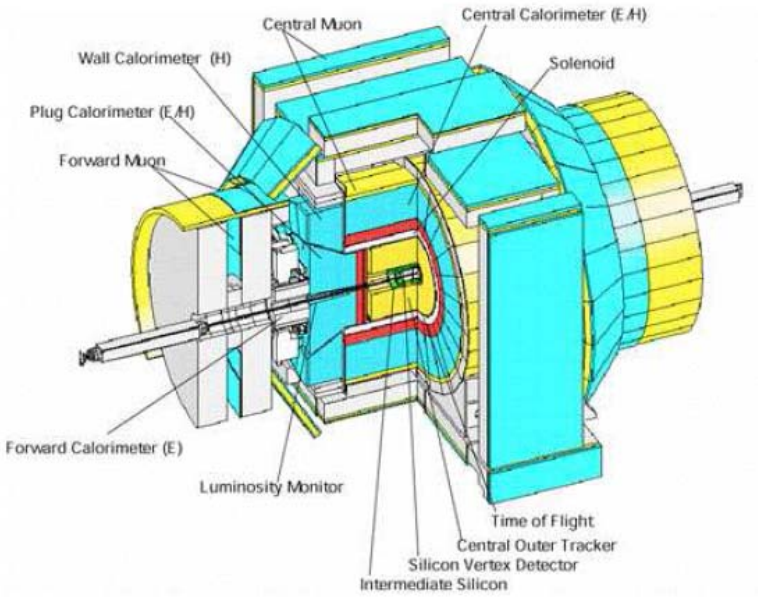

Figure 2: The cutway view of CDF detector

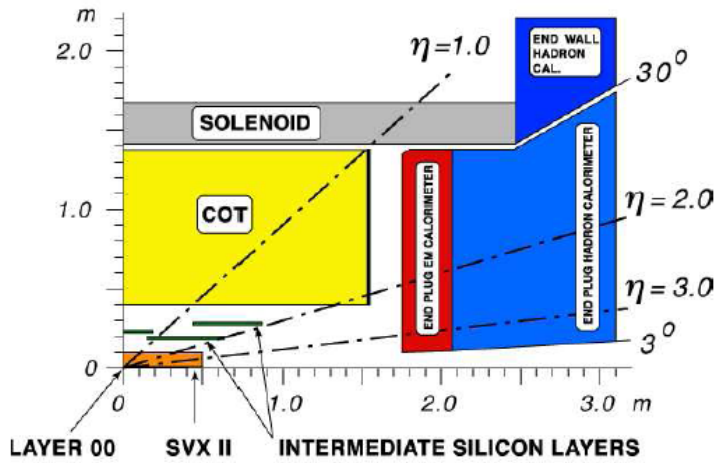

Figure 3: The longitudinal view of the CDF tracking system representing a quarter of the detector

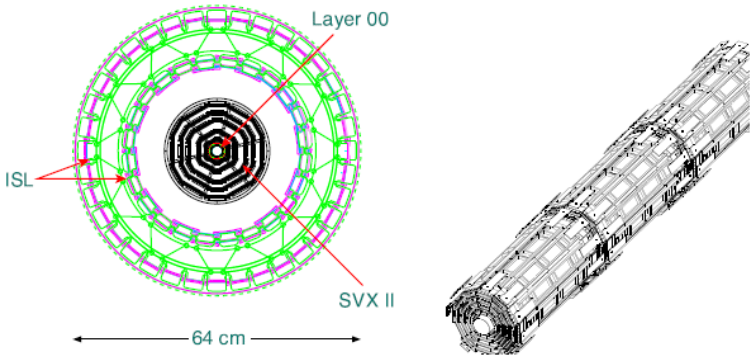

Figure 4: The silicon detector geometry in r-ϕ end view (left) and the view of three barrels of SVX II (right)

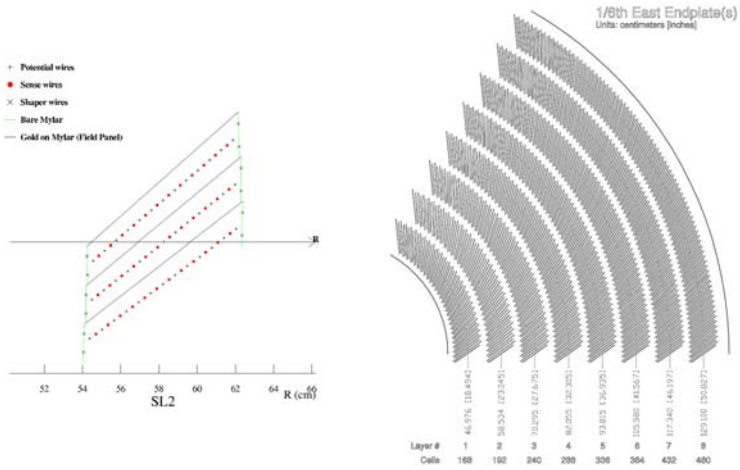

Figure 5: Three cells in COT detector along the beam direction (left) and 1/6 section of the COT end plates (right)

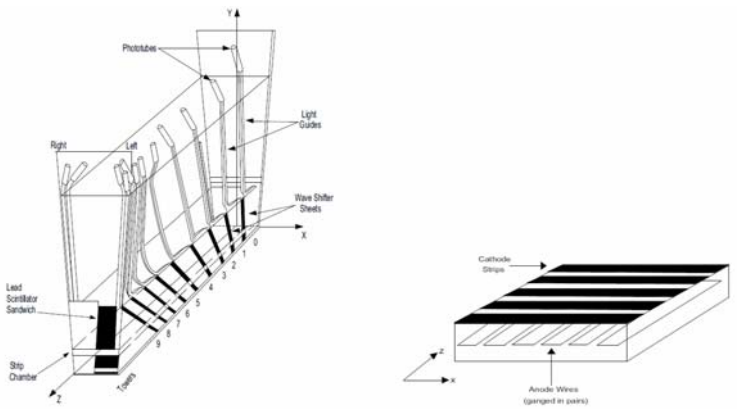

Figure 6: The single CEM wedge (left) and the central electromagnetic strip chamber (right)

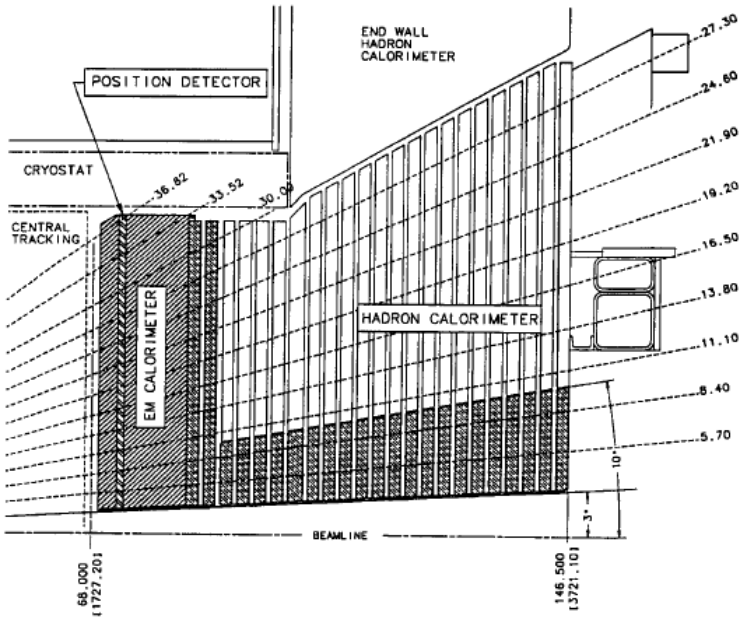

Figure 7: The cross section of plug calorimeter system

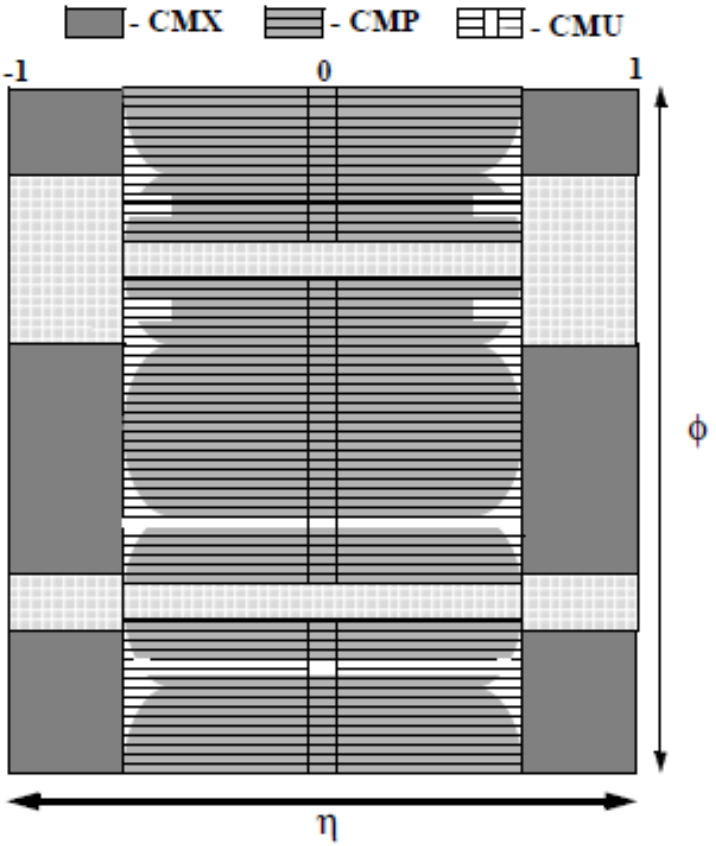

Figure 8: Muon Detector Coverage

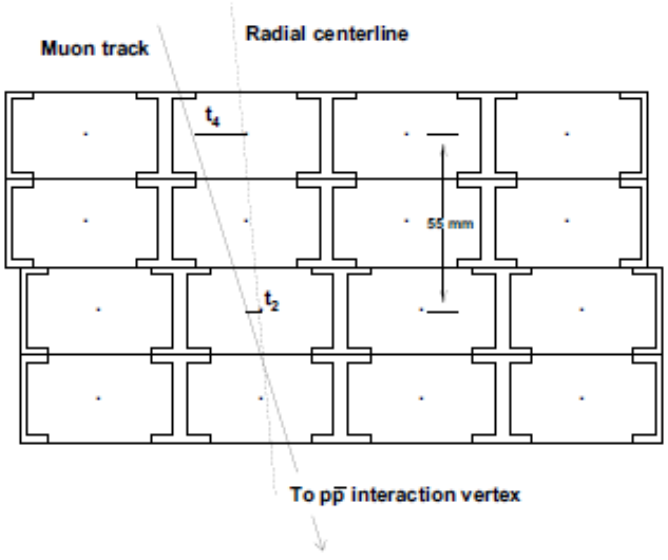

Figure 9: Cross section view of muon chamber. Each cell is filled with a gas of argon and ethane mixture. A sense wire is located at the center of cell.

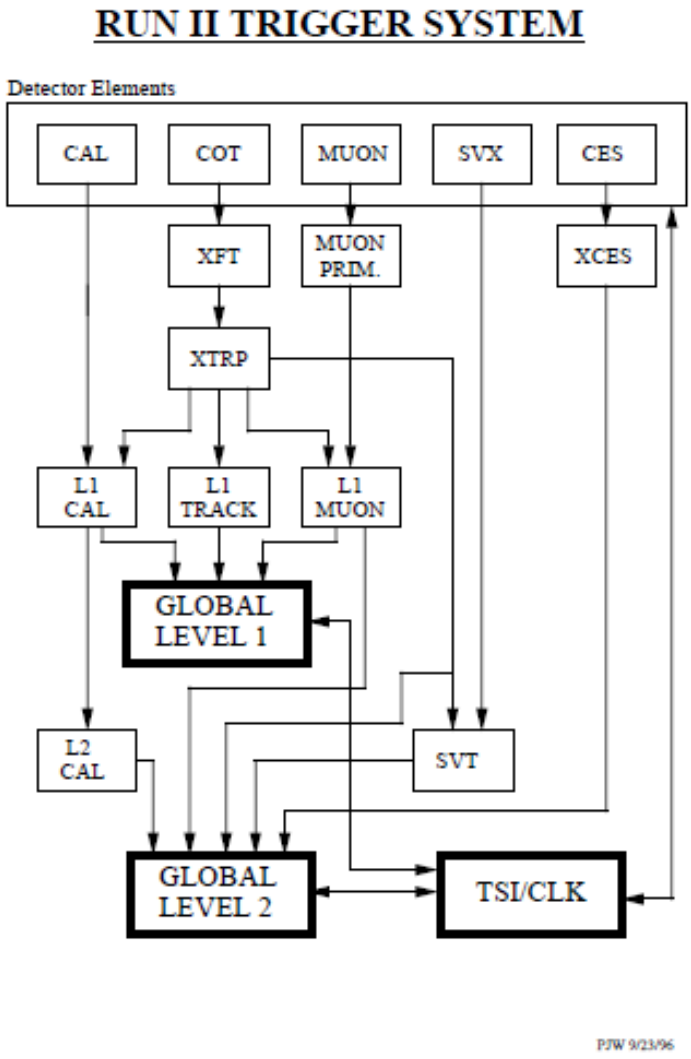

Figure 10: Trigger System

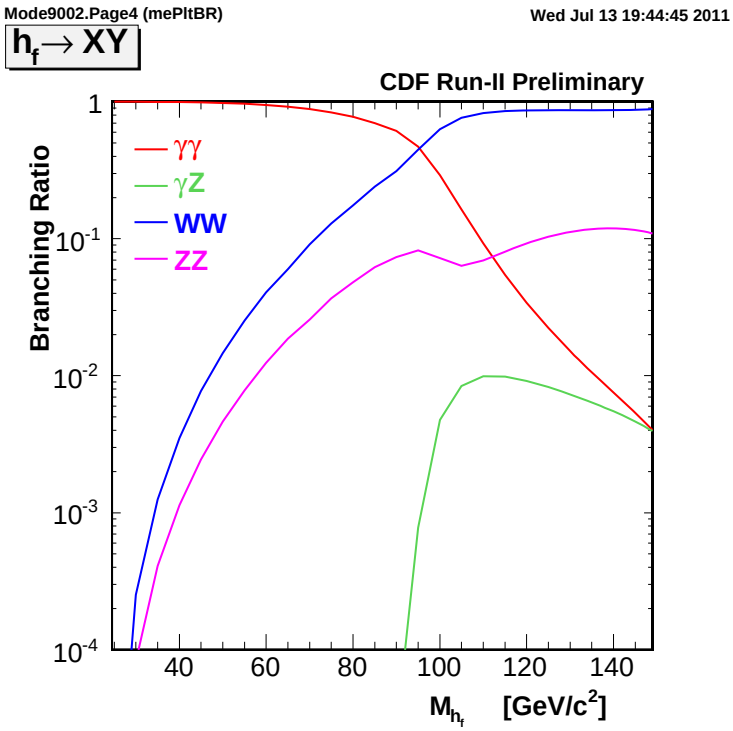

Figure 11: Branching ratios of $h_f \rightarrow XY$ ($\tan\beta = 10$)

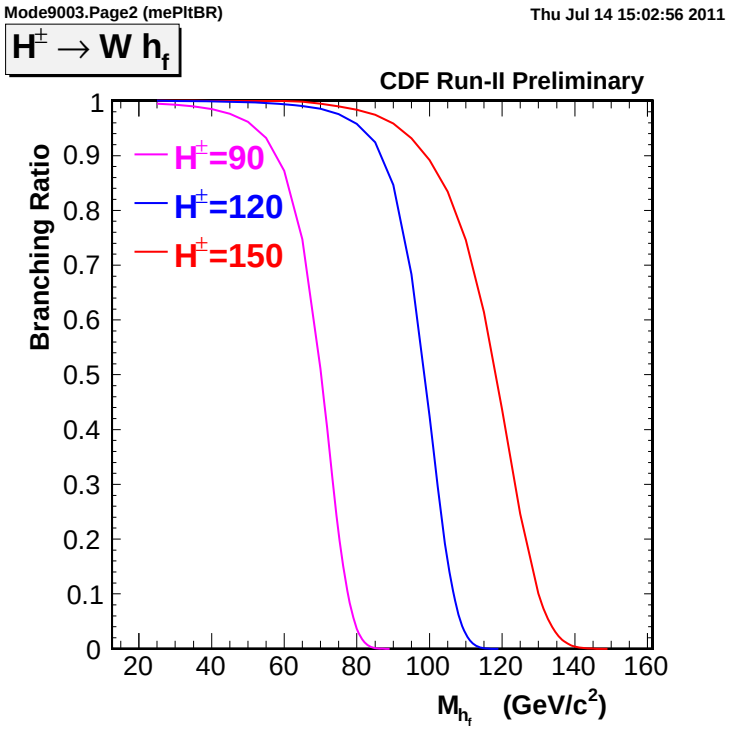

Figure 12: Branching ratios of $H^{\pm} \rightarrow Wh_f$ ($\tan\beta = 10$)

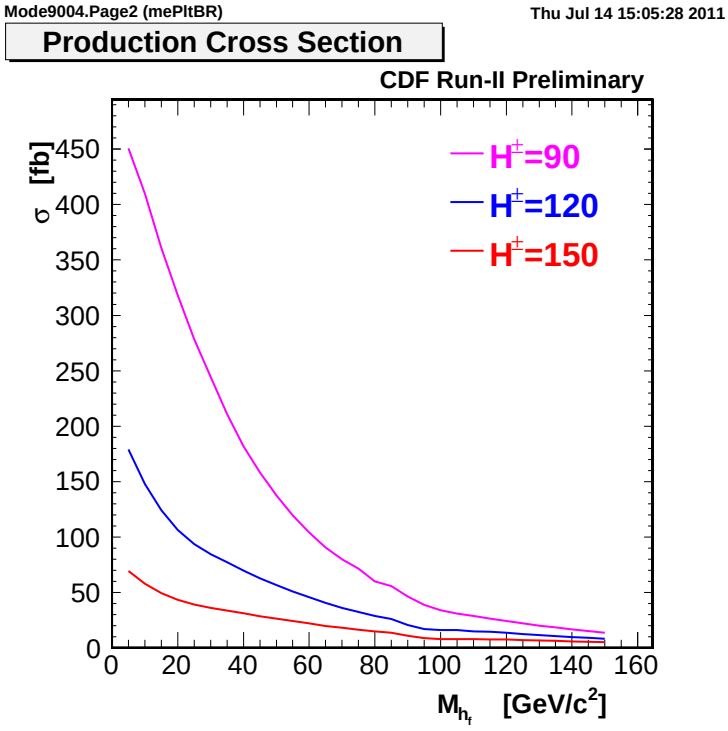

Figure 13: Production cross section ($\tan\beta = 10$)

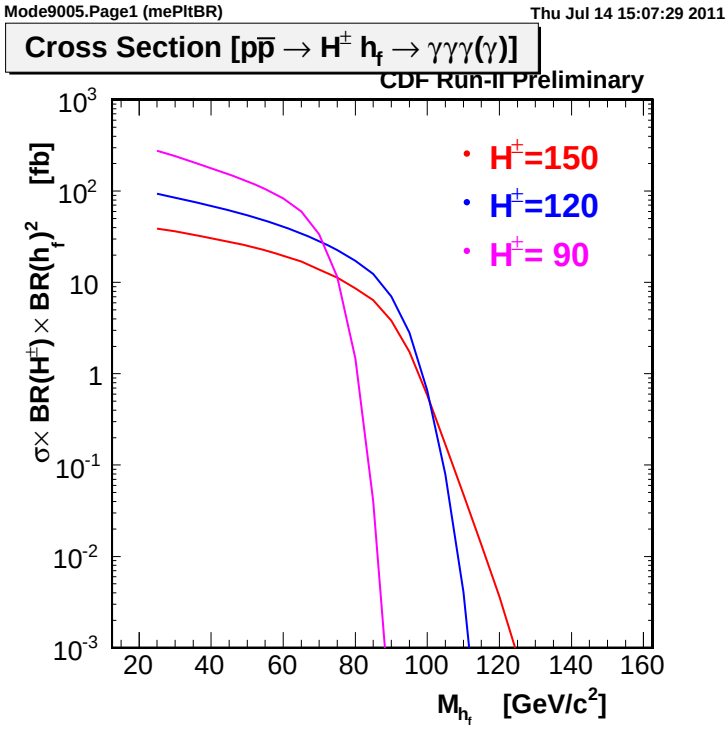

Figure 14: Cross section for $p\bar{p} \to \gamma\gamma\gamma(\gamma) + X$ ($\tan\beta = 10$)

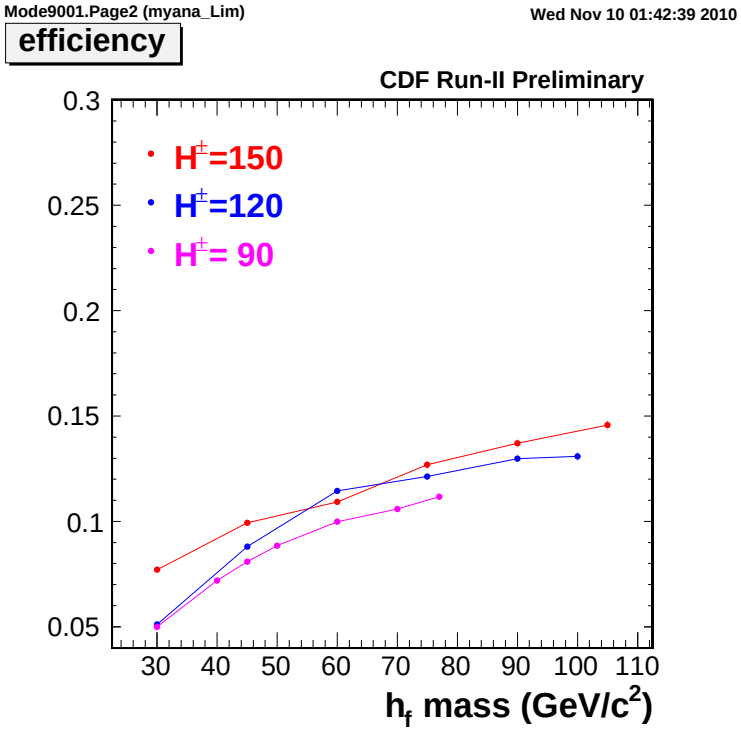

Figure 15: Efficiencies of h_f detection, showing statistical errors only.

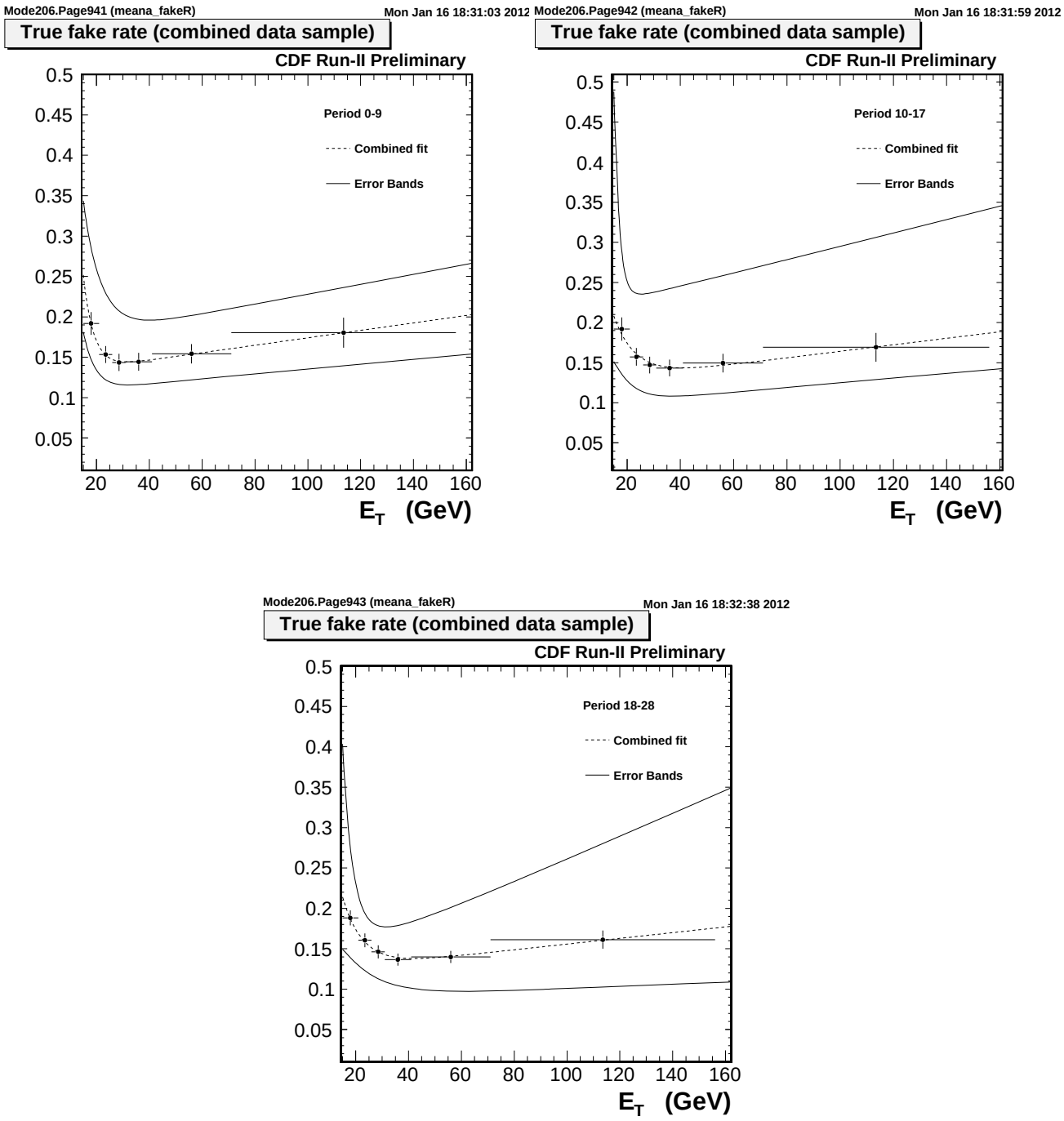

Figure 16: True fake rate for jet sample $P_{true}(\mathrm{E}_T)$ with error bands(solid), and fitting of the combined data (JET20, 50, 70, 100)(dashed).

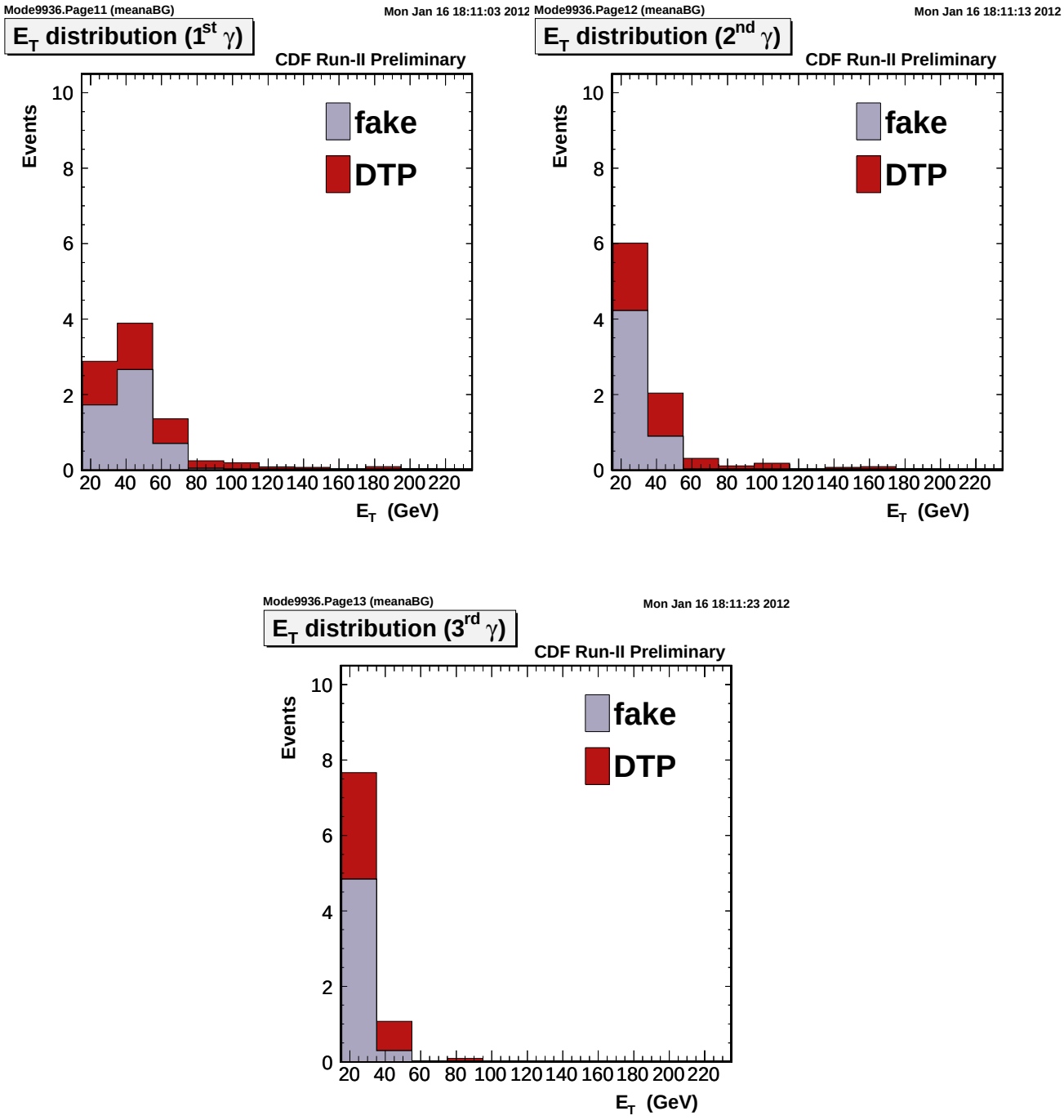

Figure 17: Distributions of each E_T for 3γ+X events expected SM background.

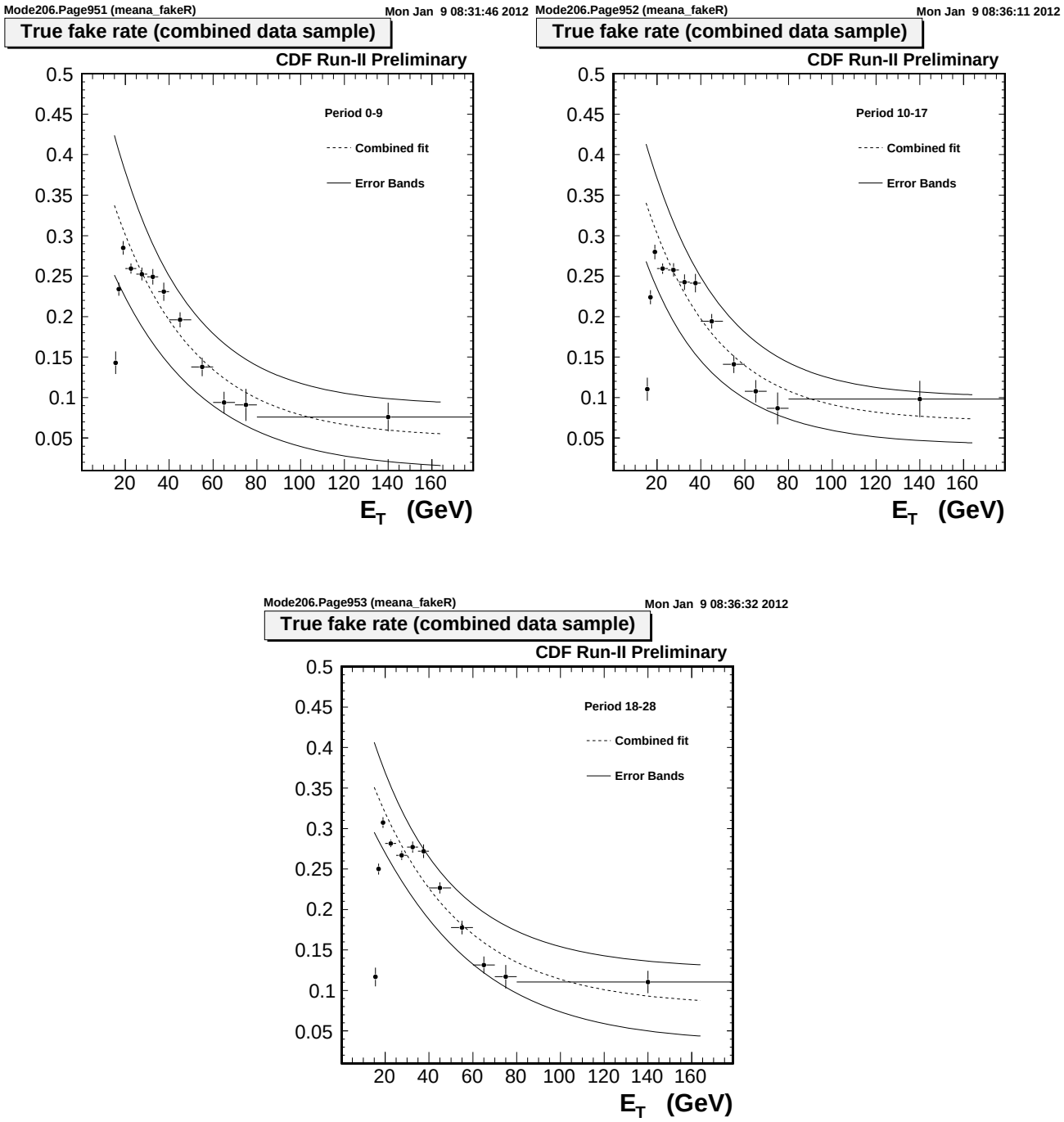

Figure 18: Fake rate for jet sample $P^{loose}(\mathrm{E}_T)$ with error bands (solid) and fitting of the combined data (JET20, 50, 70, 100)(dashed). These fake rates are made for the loose photons.

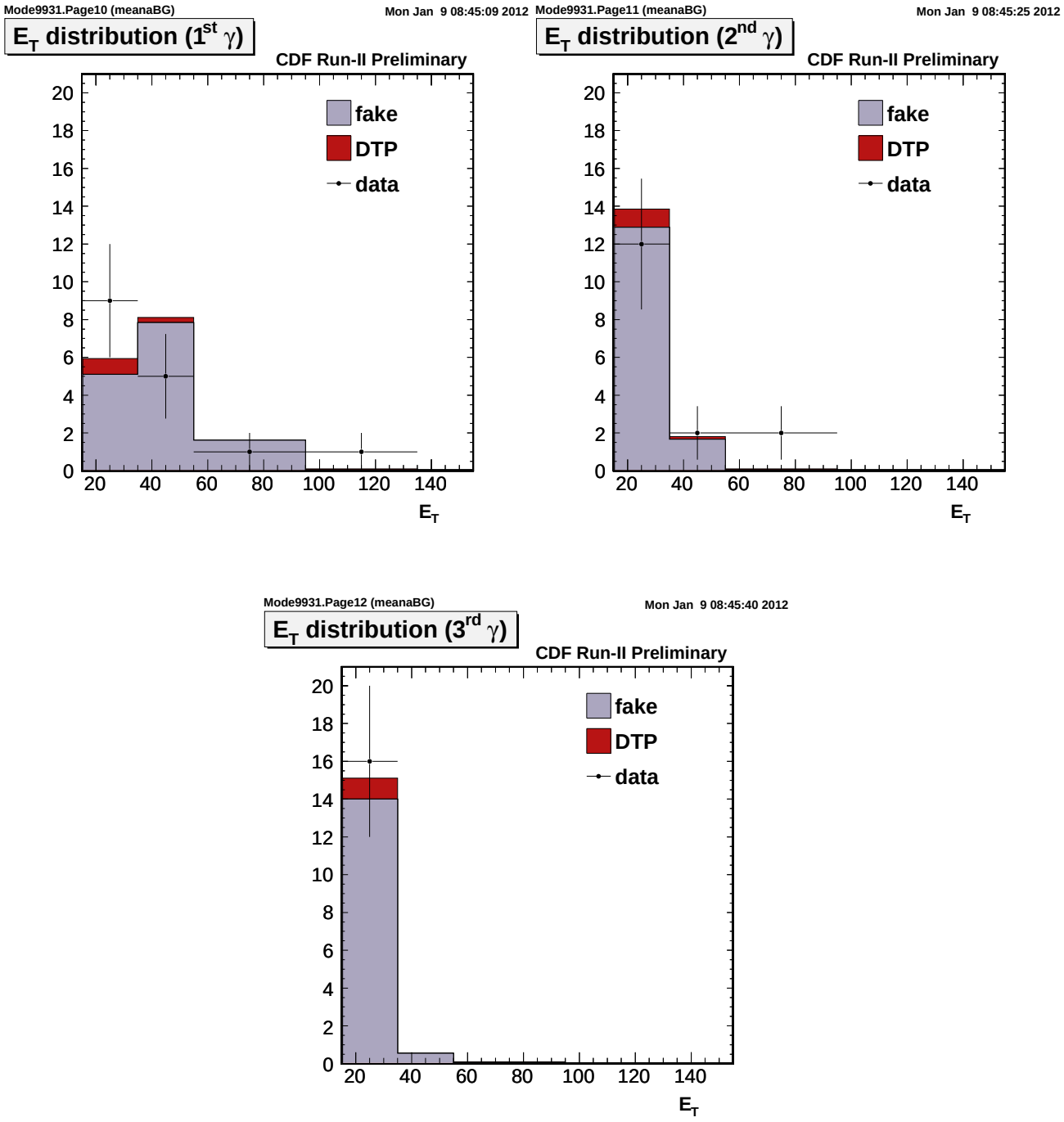

Figure 19: Distributions of each E_T in side-band event

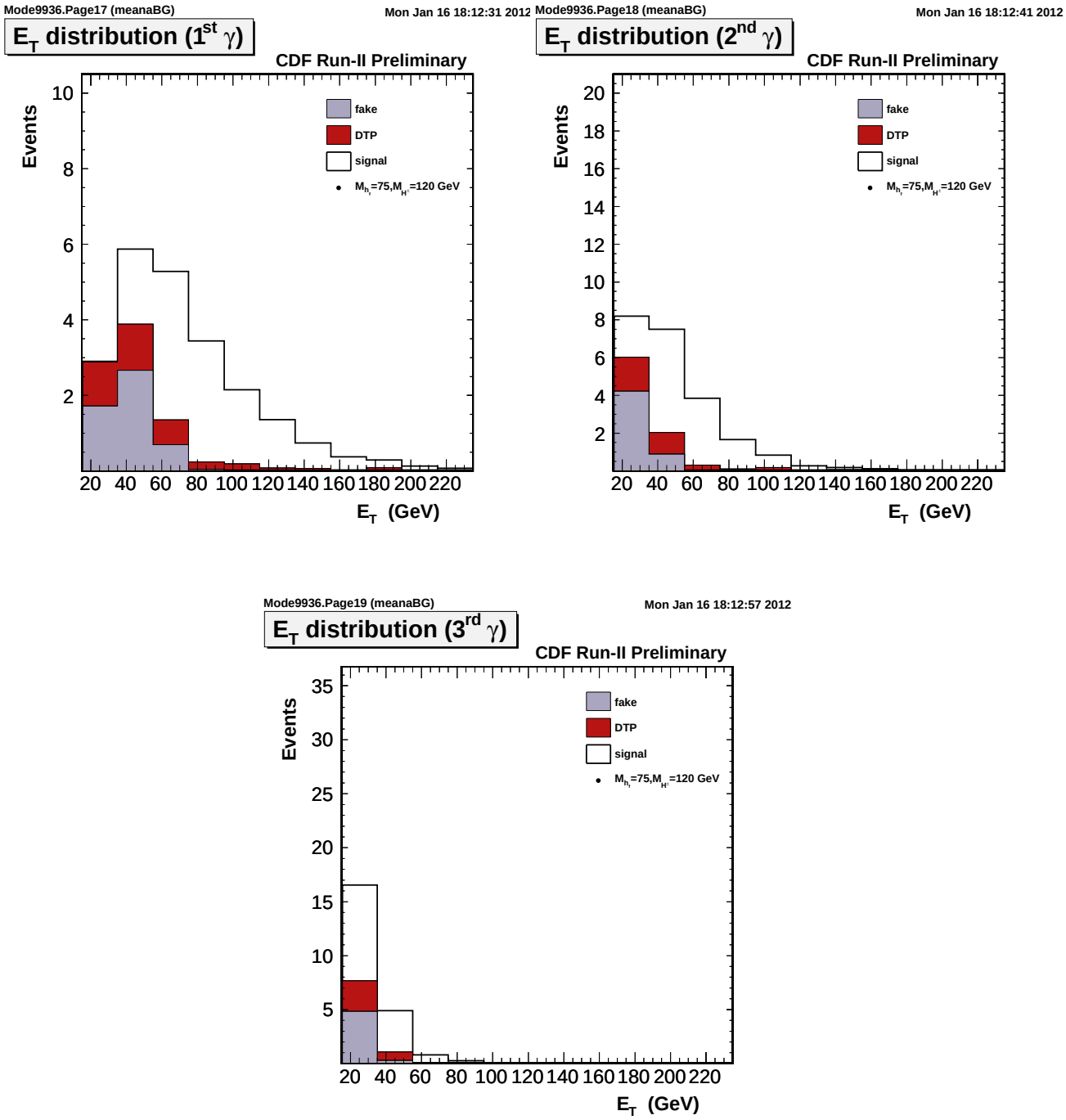

Figure 20: Distributions of each E_T for 3γ+X events expected in SM background and in signal events. We compare the background distribution before unblinding the signal region and expected signal in the signal region for an example mass of $h_f = 75$ and mass of $H^{\pm} = 120$ GeV.

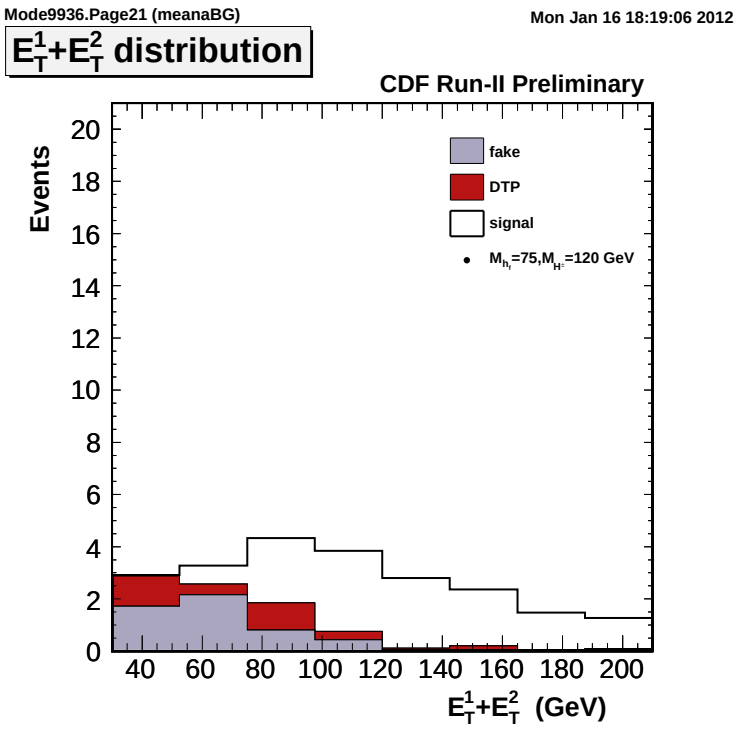

Figure 21: Distribution of $E_T^1+E_T^2$ for 3γ+X events expected in SM background and in signal events. We compare the background distribution and expected signal in the signal region for an example mass of $h_f = 75$ and mass of $H^\pm = 120$ GeV. In the region of low $E_T^1+E_T^2$, the background distribution is dominant while the background is reduced in the high $E_T^1+E_T^2$ region.

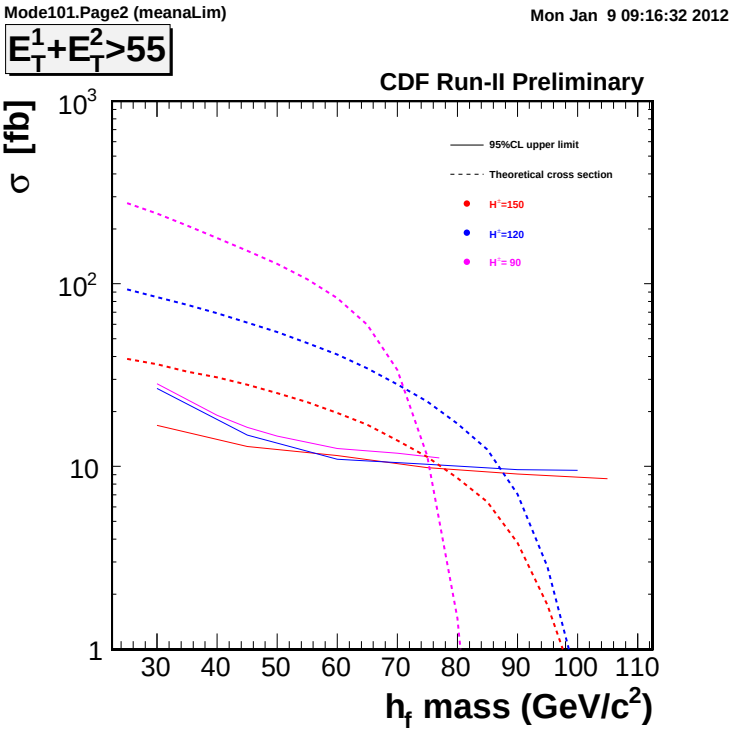

Figure 22: The expected 95% C.L. cross section limit and theoretical cross section at $E_T^1+E_T^2 > 55$. The expected 95% C.L. cross section limit is solid line and theoretical cross section is dash line. For $H^{\pm} = 90$ GeV, the excluded region is mass of h_f (M_{h_f}) < 72 GeV.

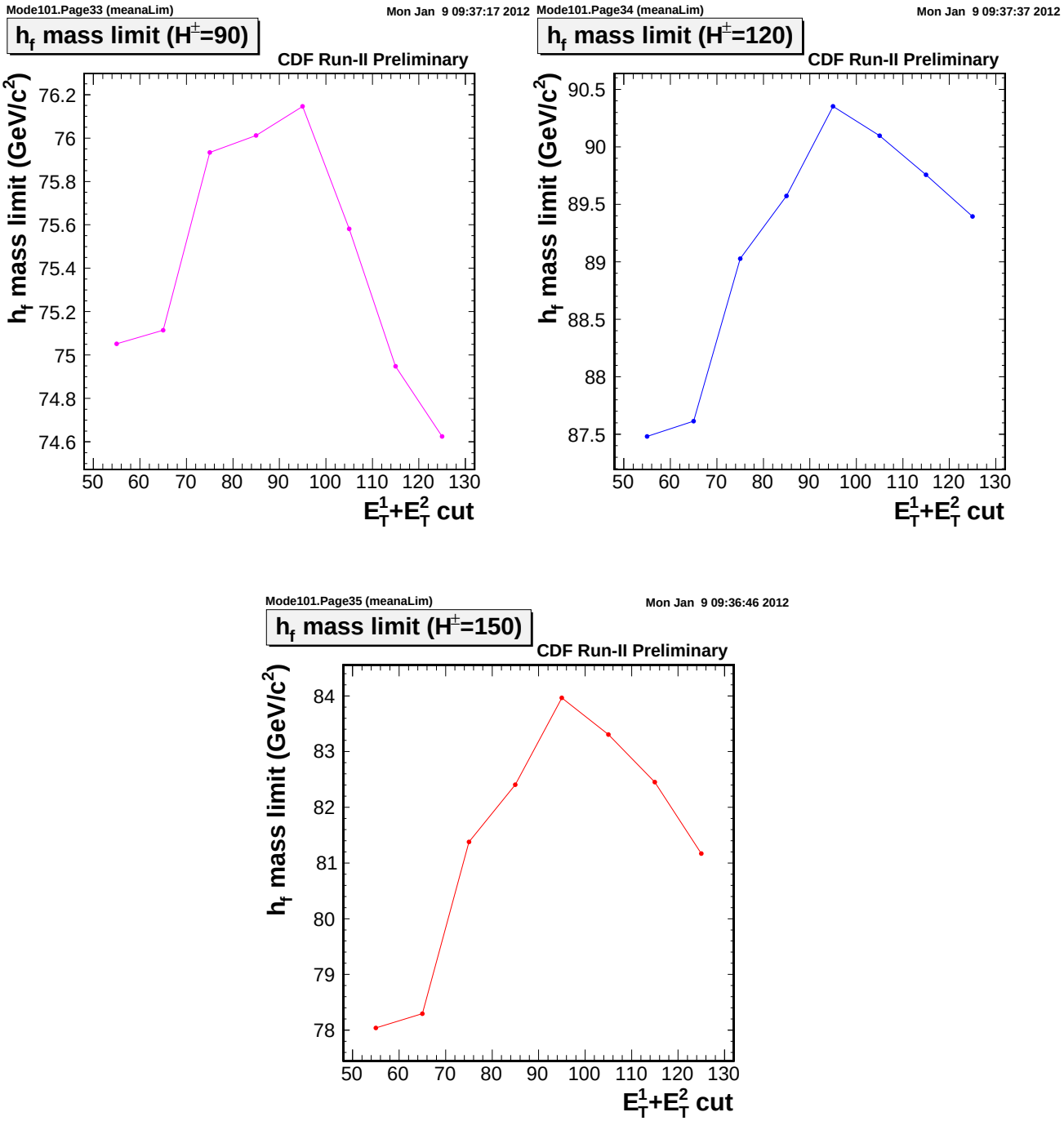

Figure 23: h_f mass limit as a function of the $E_T^1+E_T^2$ requirement. The y-axis of this plots are the intersection points between the expected 95% C.L. cross section limit and theoretical cross section. That is the excluded region of h_f mass as described 22. We choose $E_T^1+E_T^2 > 95$ GeV as this maximizes and stabilize the mass limit.

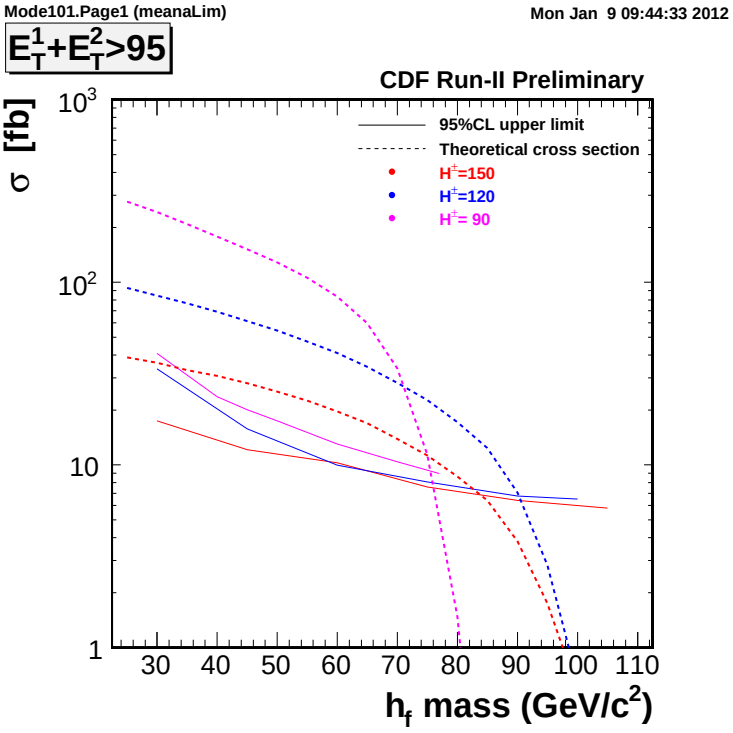

Figure 24: The expected 95% C.L. cross section limit and theoretical cross section for $E_T^1+E_T^2 > 95$. The expected 95% C.L. cross section limit is solid line and theoretical cross section is dash line.

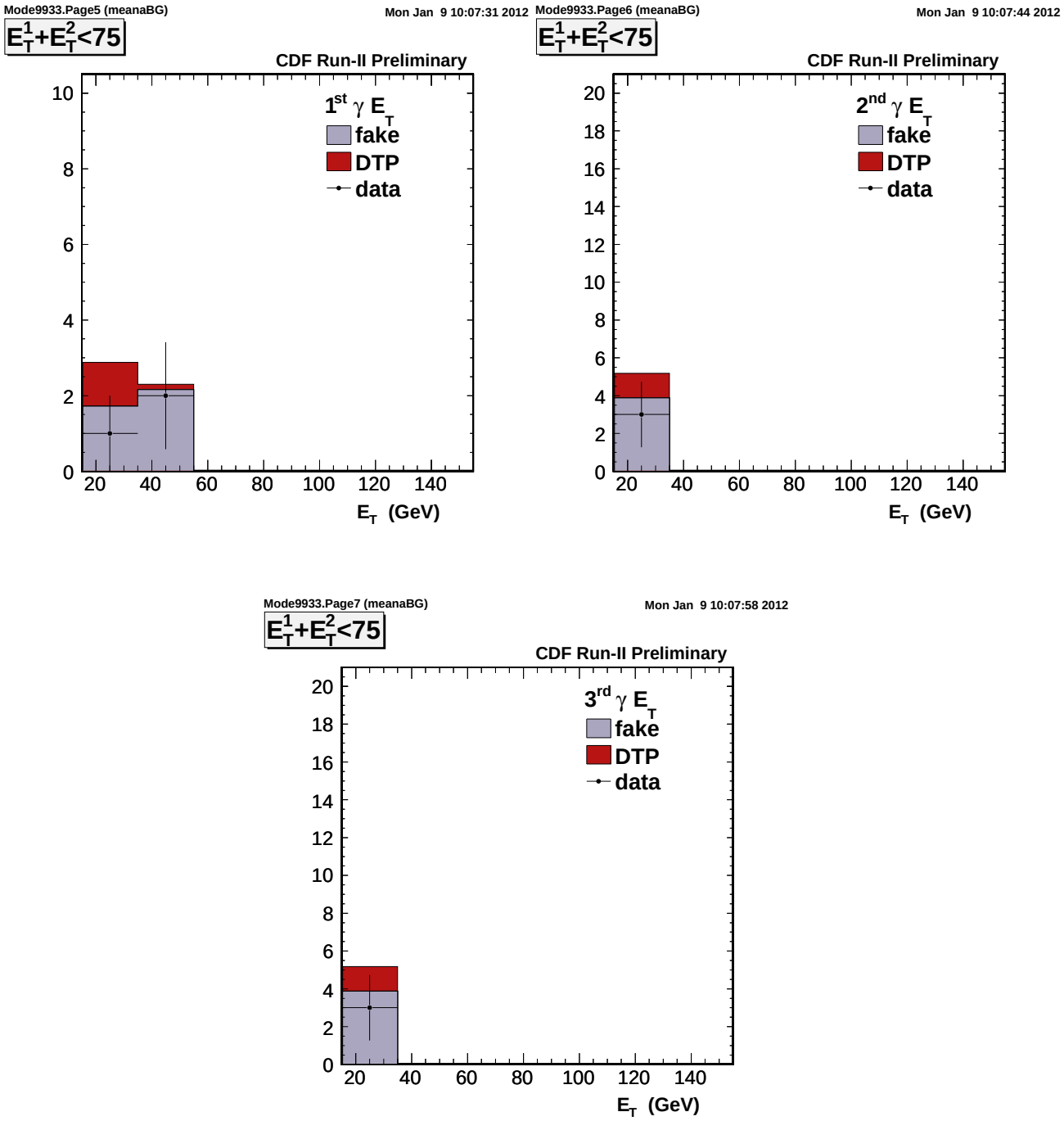

Figure 25: Distributions of each E_T for 3γ+X events expected in SM background and in signal events. We compare the background distribution before unblinding the signal region and expected signal in the signal region for an example mass of $h_f = 75$ and mass of $H^{\pm} = 120$ GeV.

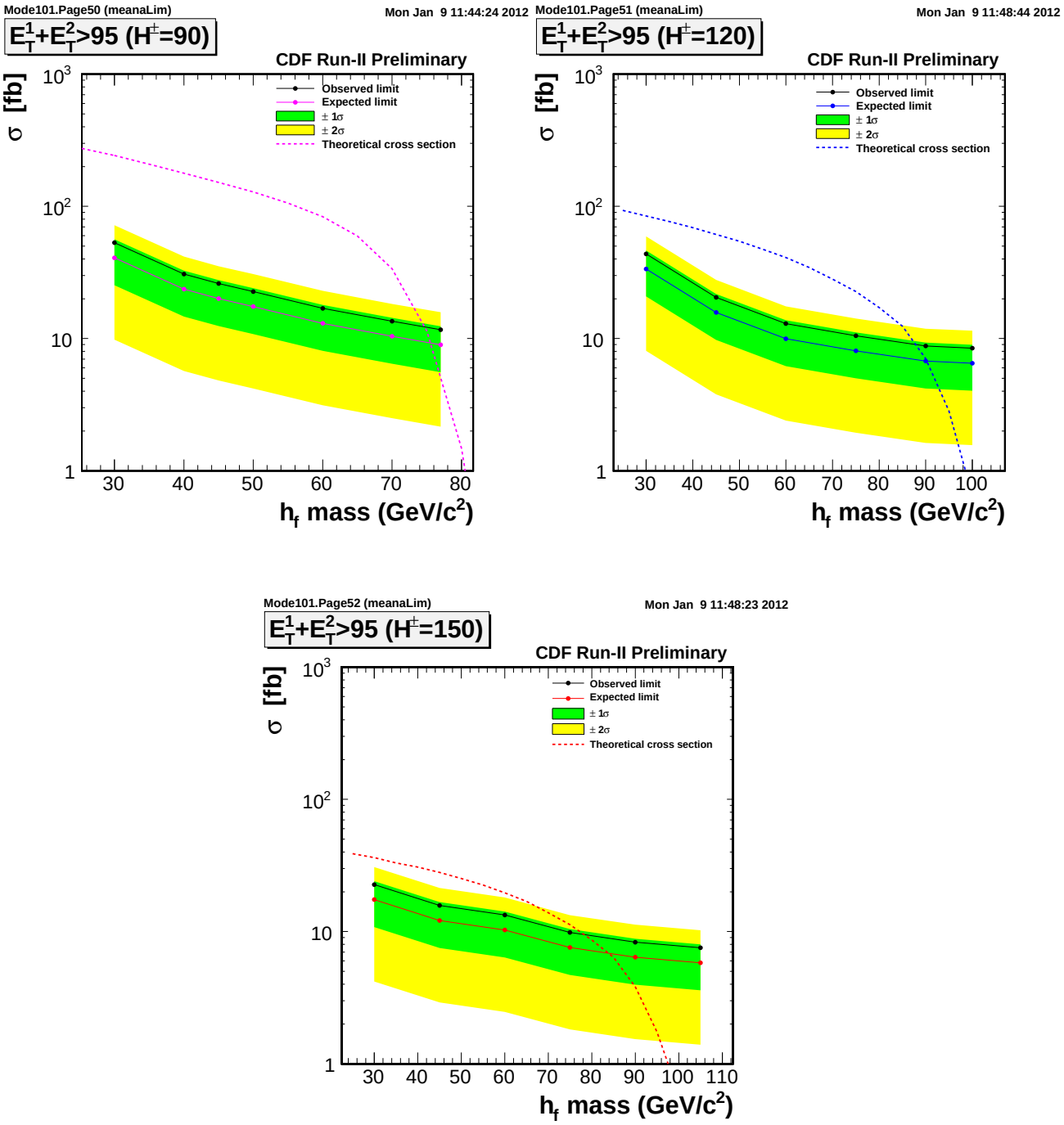

Figure 26: The upper limits on the $\sigma(p\bar{p} \to H^{\pm}h_f) \times Br(H^{\pm} \to W^*h_f) \times (Br(h_f \to \gamma\gamma))^2$ at a 95% cofidence level as a function of h_f mass.

A Appendix

The Rate of Jets Faking Photons

We estimate the rate at which a jet originating from a quark or a gluon fakes an isolated photon in the central calorimeter. We start measuring $P_{raw}(\mathrm{E}_T)$ which is simply the fraction of jets passing the standard photon cut. We must correct the raw fake rate ($P_{raw}(\mathrm{E}_T)$) by the "true" photon contamination to obtain the true fake rate. The true fake rate ($P_{true}(\mathrm{E}_T)$) is obtained by multiplying the raw fake rate ($P_{raw}(\mathrm{E}_T)$) with the F_{QCD} which is the correction factor.

A.1 Raw Fake Rate Measurement

A.1.1 Selection of QCD jets

This analysis uses jets from the Jet20, Jet50, Jet70, and Jet100 triggered data sets, filtered by the electron/muon no-silicon good run list version 35. These data sets, which range from runs 138425 to 289197, contain ≈ 6.7 fb^{-1} of integrated luminosity. We filter these QCD events by requiring that the ΔR separation between all other jets is at least 0.4. The transverse energy spectra for this jet sample are saved in the form of histograms. The jets are further subdivided into three groups from highest to lowest jet E_T: 1st jet, 2nd jet, and 3 or more jets (referred to as jet category "345th"). Note that the energy rankings use all jets before any further cuts are made on the datasets.We choose the 345th category for the raw fake photon measurement ($\mathrm{P}_{raw}(\mathrm{E}_T)$). Jets with $\mathrm{E}_T > 15$ GeV and $|\eta| < 1.1$ are considered for the central photon raw fake rate measurement.

A.1.2 Mesurement of $\mathbf{P}_{raw}(\mathbf{E}_T)$

Having determined the QCD jet sample, we search each event for the closest matching electromagnetic (EM) object to the selected jet. If the separation between has ΔR$<$ 0.4, we accept the EM object as a candidate for faking a photon.
To apply Di-photon sample we have to make the fake rate for Di-photon because of the effect of the triggers. We require the 345th category having EM object to pass the trigger selection cuts and the cuts of associated track. We use this subset as the denominator of fake rate.
Finally we apply the photon selection cuts listed in Table 5 to the matched EM objects to determine the number that would be accepted as central photons.
We parameterize the measurement of P_{raw} as a function of the jet E_T. Figure A.1 shows this raw fake rate as a function jet E_T using the 345th jet sample combined from Jet20 to Jet100 with statistical error bands (solid curves). The parameterization of these lines is given in Table A.1. An E_T-dependent shape is to be expected as the photon selection cuts depend on E_T. The value of $\mathrm{P}_{raw}(\mathrm{E}_T)$ is $\approx 0.35\%$ at the lowest

jet E_T and decreases to $\approx 0.2\%$ at 35 GeV. At this point the ability of the CES to resolve single and multiple photons is lost and the fake rate slowly rises to $\approx 0.6\%$ at ≈ 120 GeV.
Figure A.2 shows the systematic error bands on the $P_{raw}(E_T)$ measurement. As a measure of the systematic errors we make separate analysis using the different jet data sets (JET20, JET50, JET70, and JET100). We use the difference in the fake rate measured from these datasets as a systematic error bands (solid curves) shown in Figure A.2. The parameterization of these curves is given in Table A.2.

A.2 Real Photon Correction

The jet sample used to measured the raw fake rate contain "real" photons from direct production or bremsstrahlung radiation. The real photons have a high probability to pass the photon selection and thus increase the measured fake rate. A correction factor, $F_{QCD} = N(jets \rightarrow photons)/\left[N(jets \rightarrow photons) + N(photons)\right]$, which estimates the fraction of actual jets that are in our fake rate sample, is applied to the raw fake rate to correct for prompt photon contamination. Correcting the raw fake for prompt photon contamination must be accomplished by statistical methods, because particle by particle identification is not possible. In this section, we describe Isolation vs CES χ^2 method that are used to measure the F_{QCD}.

A.2.1 Isolation vs CES χ^2 Method

In a 2-dimensional distribution of the calorimeter isolation variable and CES χ^2 variable, signal events congregate in the low isolation and low χ^2 region, while background events have large isolation energy due to hadronic activity. The 2-dimensional plane of isolation vs. CES χ^2 can be divided into four regions (see Table A.3), where region C is the signal region and region D is entirely background. Assuming no correlation between the isolation energy and CES χ^2 for background events, the background in region C can be determined as:

$$\frac{N_C^{BG}}{N_A} = \frac{N_B}{N_D}$$

and

$$F_{QCD} = \frac{N_C^{BG}}{N_C} = \frac{N_B N_A}{N_D N_C}$$

A.2.2 F_{QCD} Measurement

Figure A.3 shows the mesurement of F_{QCD} using the Isolation vs. CES χ^2 method as a function of jet E_T. The fit parameter values can be seen in Table A.4. The data suggests that the raw fake rate sample possesses a small "real" photon contamination at lower energies and large "real" photon contamination at higher energies. We use the

difference in F_{QCD} measured from jet data sets (JET20, JET 50, JET70, and JET100) as a systematic error bands shown in Figure A.4. The fit parameter values can be seen in Table A.5.

A.3 True Fake Rate

We correct the raw fake rate by the "real" photon contamination to obtain the true fake rate for the QCD sample: $P_{true} = F_{QCD} \times P_{raw}$. Figure 16 shows $P_{true}(\mathrm{E}_T)$ for period 0-9, 10-17, 18-28. Combining the statistical and systematic errors in quadrature leads to the upper and lower error bands shown in Figure 16.

A.4 The Rate of Jets Faking Loose Photons

We estimate the rate at which a jet fakes a loose photon. We employ the same method above section to use the rate in section 7.2. Determining a candidate for faking a loose photon we apply the loose photon selection cuts in Table 10 and a candidate fail the standard photon selection in Table 5.
Figure 18 show the raw fake rate for loose photons ($\mathrm{P}^{loose}(\mathrm{E}_T)$). We use the difference in P^{loose} measured from jet data sets (JET20, JET 50, JET70, and JET100) as a systematic error bands shown in Figure A.5. The fit parameter values can be seen in Table **??**.

Table A.1: Raw Fake Rate (P_{raw}), Fit Paramters. The high and low error bands show statistical errors.

Period 0-9	Fit
Central Value	$0.0017x + 0.46$
High Error Band	$0.0021x + 0.46$
Low Error Band	$0.0013x + 0.46$

Period 10-17	Fit
Central Value	$0.0015x + 0.46$
High Error Band	$0.0019x + 0.46$
Low Error Band	$0.0011x + 0.46$

Period 18-28	Fit
Central Value	$0.0013x + 0.45$
High Error Band	$0.0016x + 0.45$
Low Error Band	$0.0011x + 0.45$

Table A.2: Raw Fake Rate (P_{raw}), Fit Paramters. The high and low error bands show systematic errors.

Period 0-9	Fit
High Error Band	$0.0017x + 0.49$
Low Error Band	$0.0012x + 0.42$

Period 10-17	Fit
High Error Band	$0.0022x + 0.51$
Low Error Band	$0.0015x + 0.41$

Period 18-28	Fit
High Error Band	$0.0053x + 0.41$
Low Error Band	$0.0014x + 0.36$

Table A.3: Cut values determining regions used for Isolation vs.CES average χ^2 method.

Region	$E_T^\gamma < 20$ GeV		$E_T^\gamma > 20$ GeV	
A	$\langle\chi^2\rangle_{ces} > 20$	$iso4/E_T < 0.1$	$\langle\chi^2\rangle_{ces} > 20$	$\frac{(iso4-2)}{(E_T^\gamma-20)} < 0.02$
B	$\langle\chi^2\rangle_{ces} < 20$	$iso4/E_T > 0.2$	$\langle\chi^2\rangle_{ces} < 20$	$\frac{(iso4-2)}{(E_T^\gamma-20)} > 0.06$
C	$\langle\chi^2\rangle_{ces} < 20$	$iso4/E_T < 0.1$	$\langle\chi^2\rangle_{ces} < 20$	$\frac{(iso4-2)}{(E_T^\gamma-20)} < 0.02$
D	$\langle\chi^2\rangle_{ces} > 20$	$iso4/E_T > 0.2$	$\langle\chi^2\rangle_{ces} > 20$	$\frac{(iso4-2)}{(E_T^\gamma-20)} > 0.06$

Table A.4: F_{QCD}, Fit Paramters. The high and low error bands show statistical errors.

Period 0-9	Fit
Central Value	$\exp(-0.26x + 2.4) + 0.28$
High Error Band	$\exp(-0.27x + 2.8) + 0.30$
Low Error Band	$\exp(-0.24x + 2.1) + 0.26$

Period 10-17	Fit
Central Value	$\exp(-0.12x + 0.067) + 0.27$
High Error Band	$\exp(-0.13x + 0.27) + 0.29$
Low Error Band	$\exp(-0.12x - 0.15) + 0.25$

Period 18-28	Fit
Central Value	$\exp(-0.13x + 0.29) + 0.27$
High Error Band	$\exp(-0.13x + 0.29) + 0.28$
Low Error Band	$\exp(-0.113x + 0.29) + 0.26$

Table A.5: F_{QCD}, Fit Paramters. The high and low error bands show systematic errors.

Period 0-9	Fit
High Error Band	$\exp(-0.15x + 1.1) + 0.36$
Low Error Band	$\exp(-0.22x + 1.5) + 0.24$

Period 10-17	Fit
High Error Band	$\exp(-0.54x + 7.6) + 0.45$
Low Error Band	$\exp(-0.17x + 0.41) + 0.22$

Period 18-28	Fit
High Error Band	$\exp(-0.26x + 3.2) + 0.33$
Low Error Band	$\exp(-0.081x - 0.55) + 0.20$

Table A.6: Fake Rate for loose photons (P^{loose}), Fit Paramters. The high and low error bands show statistical errors.

Period 0-9	Fit
Central Value	$\exp(-0.027x - 0.84) + 0.050$
High Error Band	$\exp(-0.028x - 0.89) + 0.070$
Low Error Band	$\exp(-0.027x - 0.79) + 0.031$

Period 10-17	Fit
Central Value	$\exp(-0.030x - 0.86) + 0.071$
High Error Band	$\exp(-0.032x - 0.90) + 0.094$
Low Error Band	$\exp(-0.029x - 0.81) + 0.047$

Period 18-28	Fit
Central Value	$\exp(-0.025x - 0.94) - 0.081$
High Error Band	$\exp(-0.025x - 0.98) - 0.096$
Low Error Band	$\exp(-0.025x - 0.89) - 0.066$

Table A.7: Fake Rate for loose (P^{loose}), Fit Paramters. The high and low error bands show systematic errors.

Period 0-9	Fit
High Error Band	$\exp(-0.028x - 0.48) + 0.064$
Low Error Band	$\exp(-0.025x - 0.82) - 0.0060$

Period 10-17	Fit
High Error Band	$\exp(-0.032x - 0.56) + 0.096$
Low Error Band	$\exp(-0.038x - 0.83) + 0.059$

Period 18-28	Fit
High Error Band	$\exp(-0.035x - 0.59) + 0.13$
Low Error Band	$\exp(-0.029x - 0.77) + 0.041$

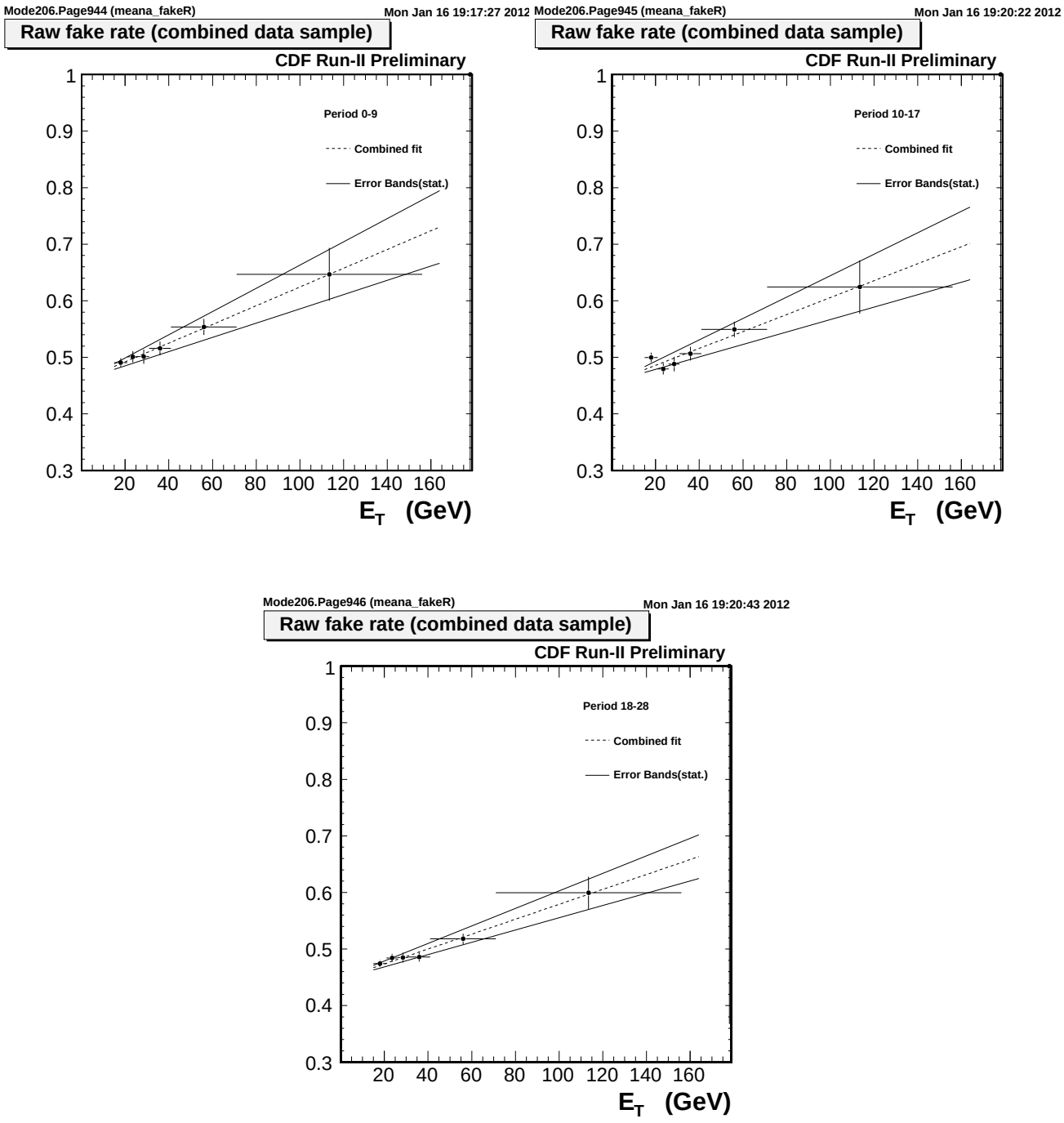

Figure A.1: Raw fake rate (P_{raw}) with statistical error bands (solid line) and fitting of combined data (JET20, 50, 70, 100)(dashed line) for period 0-9, 10-17, 18-28

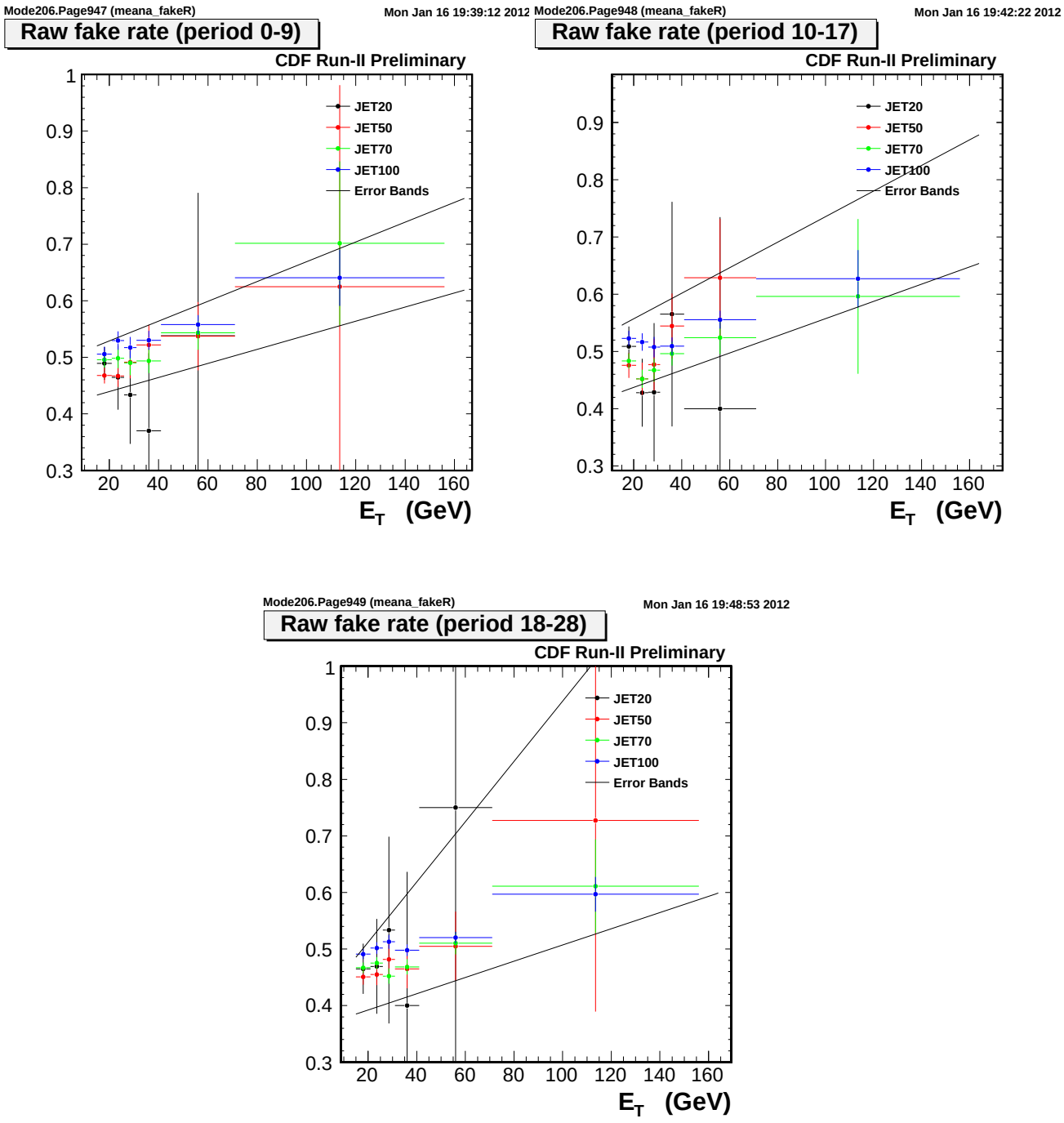

Figure A.2: Raw fake rate (P_{raw}) with systematic error bands for period 0-9, 10-17, 18-28. We use the different jet data sets (JET20, JET50, JET70, and JET100).

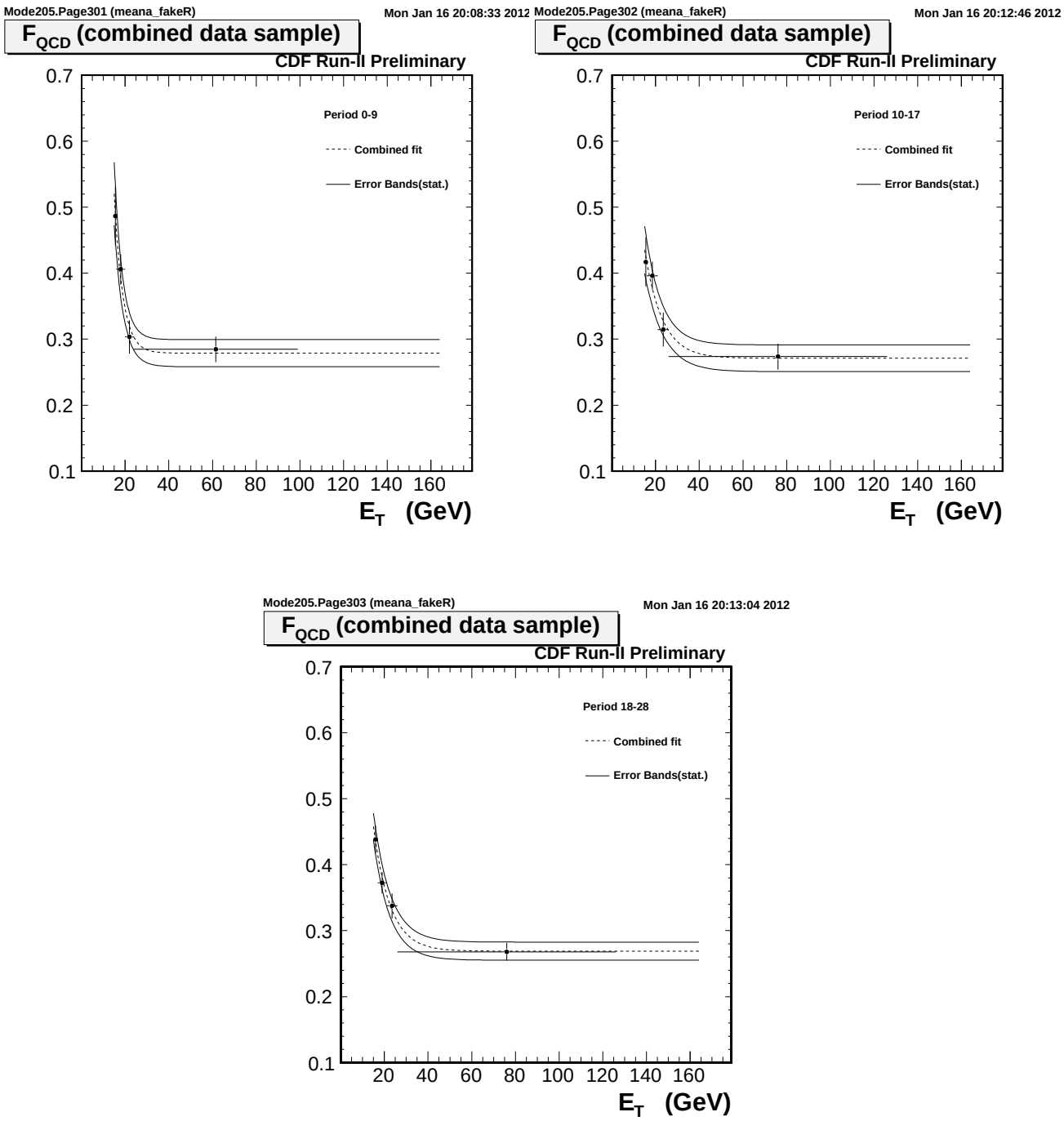

Figure A.3: F_{QCD} measurement using Isolation vs. CES χ^2 with statistical error bands for period 0-9, 10-17, 18-28.

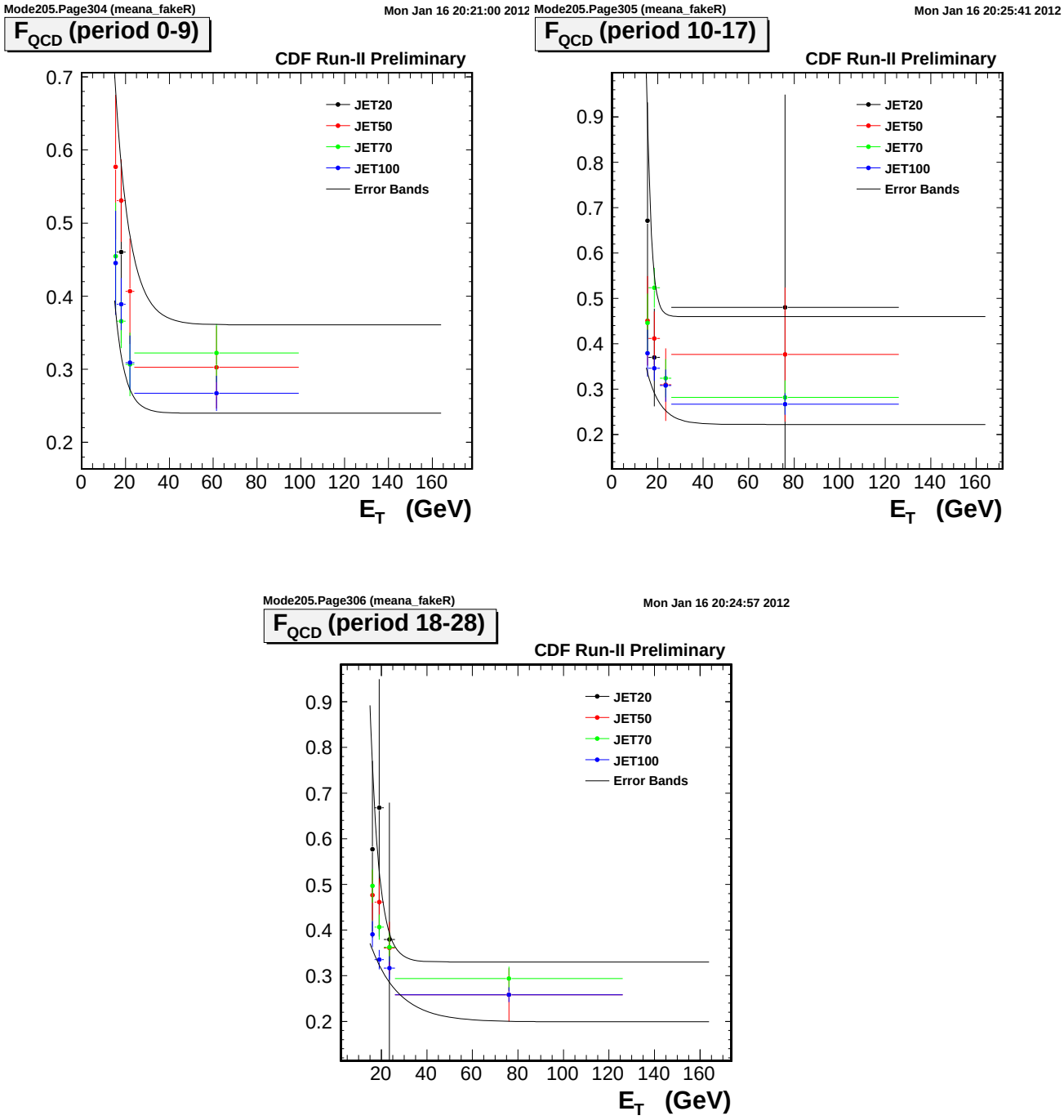

Figure A.4: Systematic error bands of F_{QCD} for period 0-9, 10-17, 18-28.

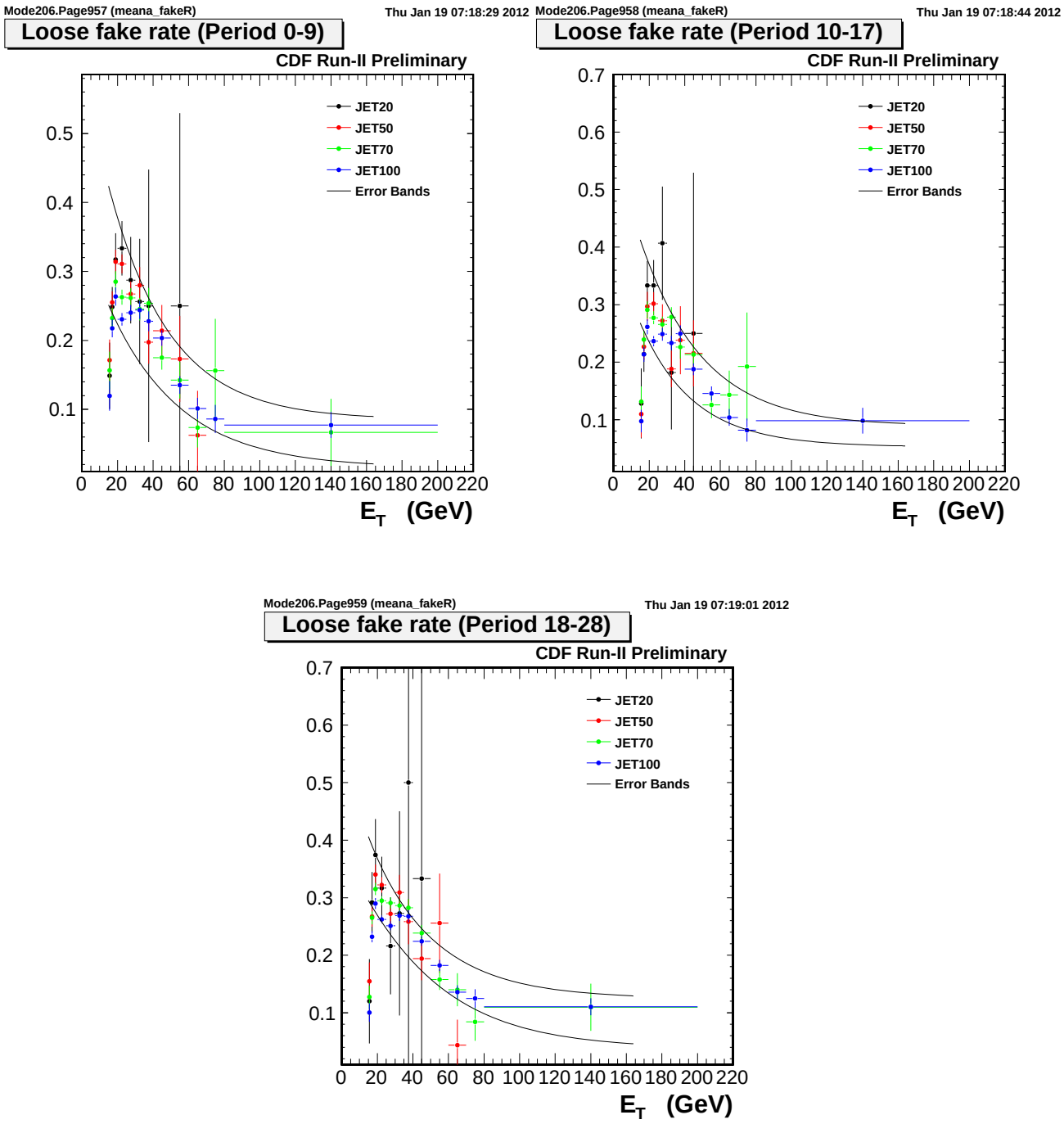

Figure A.5: Fake rate for loose photons ($P^{loose}(E_T)$) with systematic error bands for period 0-9, 10-17, 18-28. We use the different jet data sets (JET20, JET50, JET70, and JET100).

B Appendix

Photon Efficiency

B.1 Introduction

The photon identification efficiency are studied for data up to run 289197 ($\sim$ 6 fb^{-1} of integrated luminosity). Because a pure sample of photons from detector data is unavailable, the photon efficiency is calculated using efficiencies for electrons from the detector. It is assumed that electrons and photons behave similarly enough in the detector to approximate the efficiency in this way.

B.2 Data

The method applied here is taken from [27]. The CENTRAL_ELECTRON_18 high p_T electron trigger was used to select data from datasets bhel0d, bhel0h, bhel0i, bhel0j, bhel0k, and bhel0m. All runs were required to be marked good for electrons, silicon, and be included in the good run list version 35. These data sets, which range from runs 138425 to 289197.

B.3 Method

All Z→ee events are central-central data. We apply the cuts (Table B.1) to both central electron. Each event is required to have an electron passing tight cuts measured in the central detector, and one passing loose cuts in the central detector.
We fill the number of events passing the cuts and their invariant mass distributions. The signal for these events was assumed to take the form of a Gaussian distribution, and the background is taken to be linear. The signal is fixed on the range of 86 GeV to 98 GeV (roughly corresponding to a window of 12 GeV around the Z mass), and the background in the signal range is estimated by averaging the integral of the linear fit between 66 and 72 GeV and between 112 and 118 GeV. Using these fits, the number of signal events passing the cuts is estimated by subtracting the background from the Gaussian's integral.
After the number of events passing cuts is calculated using the above method, the efficiency for these events can be determined. In the case of two central electrons passing loose cuts, the analysis creates a bias that arised because of the initial requirement of one tight electron in the central detector. As one tight central electron has already been measured, the probability that the second central electron will pass tight cuts is lower. To reconcile this bias, the central-central efficiency equation must be modified.

The equation used can be seen below:

$$\epsilon = \frac{N_{TT} + N_{TT}}{N_{TL} + N_{TT}}$$

where N_{TT} is number of events with loose leg passing all tight cuts and N_{TL} is number of events with loose leg passing at least loose cuts. Table 7 shows the efficiencies for the standard photon selection. Table 11 shows the efficiencies for the photon selection of side-band events. We use the cuts of Table B.2 for side-band events. We employ these efficiencies for ϵ_s in section 6.1.1 and for ϵ_{s_l} in section **??**.

Table B.1: Central electron event selection cuts

Loose Cuts
CES fiduciality $\lvert X_{CES}\rvert \leq 21$cm, 9cm$\leq \lvert Z_{CES}\rvert \leq$230cm
$E_T > 15$
$0.9 < E/p < 1.1$
Tight Cuts
E_{Had}/E_{EM} $\leq 0.055 + 0.00045\times E$
corrected cone 0.4 Iso E_T $E_T \leq 20$: $\leq 0.1\times E_T$ $E_T > 20$: $\leq 2.0 + 0.02 \times (E_T - 20)$
χ^2(Strips+Wires)/2.0 < 20
N3D tracks in cluster ≤ 2
Track $P_T \leq 1.0 + 0.005\times E_T$ (N3D=2)
Cone 0.4 Track Iso $\leq 2.0 + 0.005\times E_T$
E_T of 2^{nd} CES cluster (wire and strip) $E_T < 18$ GeV : $\leq 0.14\times E_T$ $E_T \geq 18$ GeV : $\leq 2.4 + 0.01 \times (E_T - 20)$

Table B.2: Central electron event selection cuts for side-band events

Loose Cuts
CES fiduciality $\lvert X_{CES}\rvert \leq 21$cm, 9cm$\leq \lvert Z_{CES}\rvert \leq$230cm
$E_T > 15$
$0.9 < E/p < 1.1$
Tight Cuts
$\frac{E_{Had}}{E_{EM}} \leq 0.125$

corrected cone 0.4 Iso E_T	
$E_T \leq 20$	$\leq 0.15 \times E_T$
$E_T > 20$	$\leq 3.0 + 0.02 \times (E_T - 20)$

N3D tracks in cluster ≤ 2
Track $P_T \leq 0.25 \times E_T$ (N3D=2)
Cone 0.4 Track Iso ≤ 5.0

References

[1] C. Amsler *et al* (Particle Data Group), "Review of Particle Physics", Phys. Lett. B **667**, 1 (2008).

[2] F. Halzen and A.D. Martin, "Quarks and Leptons: An Introductory Course in Modern Particle Physics", ISBN 0-471-88741-2 (1984)

[3] S. Glashow, "Partial Symmetries of Weak Interactions", Nucl. Phys. 22 (1961) 579.

[4] S. Weinberg, "A Model of Leptons", Phys. Rev. Lett. **19** (1967) 1264.

[5] A. Salam, in "Elementary Particle Theory", ed N. Svartholm, Almqvist and Wiksells, Stockholm (1969) p.367.

[6] P.W. Higgs, "Broken Symmetries, Massless Particles and Gauge Fields", Phys. Lett. **12** (1964) 132-133.

[7] P.W. Higgs, "Broken Symmetries and The Masses of Gauge Bosons", Phys. Rev. **13** (1964) 508-509.

[8] P.W. Higgs, "Spontaneous Symmetry Breakdown without Massless Bosons", Phys. Rev. **145** (1966) 1156-1163.

[9] J.F. Gunion, H.E. Haber, G. Kane, and S. Dawson, "The Higgs Hunter's Guide", ISBN: 0-7382-0305-X (2000)

[10] J.F. Gunion and H.E. Haber, "CP-conserving two-Higgs-doublets model: The approach to the decoupling limit", Phys. Rev. D **67** (2003) 075019.

[11] The CDF II Collaboration, "The CDF II Detector Technical Design Report", FERMILAB-Pub-96/390-E (1996).

[12] T.K. Nelson *et al*, "The CDF Layer 00 Detector", FERMILAB-CONF-01/357-E (2001).

[13] C.S. Hill *et al*, "Initial experience with the CDF layer 00 silicon detector", Nucl. Instrum. and Meth. A **511** (2003) 118-120.

[14] A. Sill *et al*, "CDF Run II silicon tracking projects", Nucl. Instrum. and Meth. A **447** (200) 1-8.

[15] A. Affolder *et al*, "Status report of the Intermediate Silicon Layers detector at CDFII", CDF Public Note 5687 (2001).

[16] T. Affolder *et al*, "CDF Central Outer Tracker", CDF Public Note 6267 (2003).

[17] L. Balka *et al*, "The CDF Central Electromagnetic Calorimeter", Nucl. Instrum. Meth. A **267**, 272 (1988).

[18] S. Bertolucci *et al*, "The CDF Central and Endwall Hadron Calorimeter", Nucl. Instrum. Meth. A **267**, 301 (1988).

[19] Y. Seiya *et al*, "The CDF plug upgrade electromagnetic calorimeter test beam results", Nucl. Instrum. Meth. A **480** (2002) 524-546.

[20] D. Acosta *et al*, "The CDF Cherenkov luminosity monitor", Nucl. Instrum. Meth. A **461** (2001) 540-544.

[21] D. Acosta *et al*, "The performance of the CDF luminosity monitor", Nucl. Instrum. Meth. A **494** (2002) 57-62.

[22] H.E.Haber, G.L.Kane, and T.Sterling, Nucl. Phys. B161, 493 (1979).

[23] A. Stange, W.J. Marciano, and S. Willenbrock, Phys. Rev. D 49, 1354 (1994).

[24] M.A. Diaz and T.J. Weiler, hep-hp/9401259.

[25] M. Dorigo and Shin-Shan Eiko Yu,
"Diphoton Trigger Efficiency Study in 3 fb^{-1} of CDF II data", CDF Note 9533.

[26] C. Lester, J. Deng, A. Goshaw, B. Heinemann, A. Nagano, T. Phillips,
"Measurement of the Rate of Jets Faking Central Isolated Photons Using 1 fb^{-1} of Data", CDF9033.

[27] C. Group, R. Culbertson, J. Ray,
"Photon Efficiency Scale Factors", CDF Note 9429.

[28] http://www-cdf.fnal.gov/internal/physics/photon/docs/cuts.html

[29] R. Rossin, CDF Detector Lectures:
"Systematics on the Luminosity Measurement",
http://fcdfwww.fnal.gov/internal/WebTalks/Archive/
0410/041007_clclum_detector_lecture/04_041007_clclum_detector_lectrue
_Roberto_Rossin_1_RobertoCLC_detector-04-10-07.pdf;
S. Klimenko, J. Konigsberg and T.M. Liss, FERMILAB-FN-0741 (2003).

[30] O. Gonzalez and C. Rott,
"Uncertainties due to the PDFs for the gluino-sbottom search", CDF Note 7051 (2005).

[31] http://www-cdf.fnal.gov/internal/physics/joint-physics/agenda/20050527-minutes.html

[32] Luc Demortier,
"Objective Bayesian Upper Limits for Poisson Processes", CDF5928 (version 2.10).